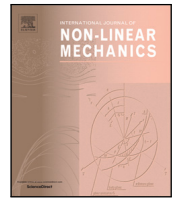




Contents lists available at ScienceDirect

International Journal of Non-Linear Mechanics

journal homepage: www.elsevier.com/locate/nlm

Substantial frequency conversion at long-wavelength limit in metamaterial with weakly nonlinear local electromechanical resonators: Analytical, computational, and experimental study

Mohammad Bukhari, Oumar Barry*

Department of Mechanical Engineering, Virginia Tech, Blacksburg, VA 24061, United States of America

ARTICLE INFO

Keywords:

Metamaterials
Energy harvesting
Perturbation techniques

ABSTRACT

Recent studies of nonlinear metamaterials have shown interesting wave propagation phenomena including the birth of soliton, tunable bandgap, acoustic nonreciprocity and broadband energy harvesting. However, most studies are limited to nonlinear mechanical metamaterials and their applications in the short-wavelength limit. There is no study of nonlinear electromechanical metamaterials at the long-wavelength limit. The present work fills this gap through investigating a metamaterial with nonlinear local electromechanical resonators. An approximate analytical solution for the dispersion relations is obtained by the method of multiple scales (MMS). This analytical solution is used to study the role of different system's mechanical and electromechanical parameters on the band structure. Other important nonlinear wave propagation characteristics are deduced by exploring the spectro-spatial features through different signal processing methods of the numerical results. The output voltage results demonstrate a significant wave distortion and frequency shift, particularly at the long-wavelength limit and other wavelength limits. The numerical results also show the birth of solitary waves and significant increase in the output voltage. Computational study via COMSOL Multiphysics and physical experiments are carried out to qualitatively demonstrate the theoretical findings. The overall observations suggest that the proposed nonlinear electromechanical metamaterial can enhance sensing and increase the operation range of electromechanical diode.

1. Introduction

Recent studies have shown that artificially engineered structures can offer exceptional properties that cannot be obtained by conventional homogeneous structures [1]. These structures are usually called metamaterials. The exciting properties of metamaterials include, but are not limited to: negative stiffness, negative mass, negative Poisson's ratio, and negative density (i.e., negative is associated with the effective parameter not to the parameter itself) [2]. The study of mechanical metamaterial was initially motivated by the development within the optics community [3]. Then, it was extended for acoustics [4] and elastic wave applications [1]. The unique characteristics of the mechanical metamaterial allow it to control noise and vibration, harvest energy, enable non-reciprocal wave propagation devices, and non-destructive testing.

For vibration attenuation applications, metamaterials draw their interesting properties from periodicity [5] (i.e., phononic crystals) or through the embedded local resonators [6]. Periodic structures offer a low-frequency bandgap where waves with a wavelength near the lattice constant cannot propagate through the structure [5,7–11].

This bandgap results from Bragg scattering. However, the limitations associated with the lattice dimension limit the application to large structures, and thus controlling smaller size structures requires different engineering configurations. This limitation can be overcome by embedding local resonators in locally resonant metamaterials by mode hybridization. This configuration showed the ability to attenuate waves with wavelengths much larger than the lattice constant [6]. Also, in the presence of periodicity, locally resonant metamaterials can form bandgaps due to Bragg scattering and mode hybridization depending on the structure and local resonators parameters [12]. Yet bandgaps can be generated without Bragg scattering at a very low local resonator's frequency. Therefore, locally resonant metamaterials can also offer a frequency bandgap even in the absence of periodicity [13]. It is noteworthy that multiple tuned frequency bandgaps can be obtained by utilizing different resonance frequency local resonators [14,15].

With increasing amplitude of a wave propagating in an inherently nonlinear medium, the linear equation cannot adequately describe the problem, and nonlinear terms need to be considered. Nonlinear metamaterials can be handled using different techniques depending on

* Corresponding author.

E-mail address: obarry@vt.edu (O. Barry).

the strength of nonlinearity. For weak nonlinearity, perturbation methods can be utilized to obtain an approximate converging closed-form solution [16,17]. For example, Narisetti et al. utilized the Lindstedt-Poincare technique to obtain dispersion relation in discrete metamaterial [18,19]. The obtained nonlinear dispersion relations were also demonstrated experimentally in [20]. Moreover, the method of multiple scales (MMS) can handle more complex problems that include nonlinear interaction of multiple waves [21]. MMS can better address the problem by reducing the required efforts associated with the algebra. Also, MMS is more convenient in handling higher-order perturbation [22]. These perturbation techniques can be further extended for 2D metamaterials [23–26]. On the other hand, strong nonlinearity in metamaterial can be treated by other techniques like homotopy analysis [27–29]. In addition to the accuracy obtained by considering nonlinear metamaterial, nonlinear metamaterials show interesting wave propagation phenomena beyond those observed in linear metamaterials, such as solitons [30,31], non-reciprocal wave propagation [32,33], second harmonic generation [34,35], and tunable bandgaps [36]. Furthermore, locally resonant nonlinear metamaterials have demonstrated that additional chaotic bandgaps can broaden the isolation band through nonlinear local resonators [37], or bridging coupling between nonlinear local resonators [38]. Other forms of nonlinearity in the local resonator have also demonstrated improvement in the bandgap size. For instance, impact based [39] and bistable [40] local resonators can broaden the conventional bandgap associated with linear resonator. Improvement in the bandgap size in nonlinear metamaterials was also demonstrated through electromechanical [41] and electromagnetic [35,42] interactions.

The study of nonlinear metamaterials has been limited to obtaining the cut-off frequency through deriving the dispersion relations or investigating solitary waves at a short-wavelength limit. These investigations do not reveal the essential characteristics of the nonlinear wave propagation in metamaterials. Therefore, several studies in the literature employed spectro-spatial analysis to provide a better understanding of these essential properties [43–47]. Spectro-spatial features can provide detailed information on the local wave properties (e.g., solitary waves) or global wave properties (e.g., dispersion curves). Studies on spectro-spatial analyses have included studies on nonlinear periodic chains [43], nonlinear locally resonant metamaterial [44], and locally resonant metamaterial with multiple local resonators with nonlinearity stemming from the chain or resonators [45–47]. These studies demonstrated the birth of solitary waves at short-wavelength limit, a significant frequency conversion at medium-wavelengths for transient excitation, and no effect of nonlinearity at long-wavelength limit in the case of the nonlinear chain [46]. Moreover, the investigations revealed that wave distortion could be obtained at all wavelength limits in the case of nonlinear resonator depending on the resonance frequency of the nonlinear local resonator [45–47]. These frequency shifts indicate that such nonlinear metamaterial can enable the design of acoustics diodes.

In addition to the superior performance of metamaterial in vibration attenuation, recent studies were motivated by the wide plateau band of frequencies in metamaterials to harvest energy [48]. The energy harvesting can be realized by installing electromechanical resonators instead of conventional local resonators for simultaneous energy harvesting and vibration attenuation [49]. Although earlier consideration of electromechanical coupling was to generate piezoelectric bandgap through the added stiffness [41,50–54], recent investigations showed the possibility of harvesting additional energy through this coupling [48,49,55,56]. These investigations were conducted experimentally on locally resonant phononic plates [48] and 2D metamaterials [57], or theoretically on discrete systems [49], continuous systems [55], and coupled internal resonators [56].

To the best of our knowledge, recent studies on metamaterials for simultaneous energy harvesting and vibration mitigation were limited to investigating the linear problem. Only our previous work in [58]

considered the effect of nonlinearity in such a problem. However, the nonlinearity in our previous work stems only from the nonlinear chain. This restricts the effect of nonlinearity for only short-wavelength limits, thus limiting the system applications to frequencies in this region (e.g., acoustics diodes, significant frequency shift). There is a gap in the literature in extending nonlinear metamaterial's applications to frequencies at all wavelength limits in the presence of nonlinear electromechanical resonator for simultaneous energy harvesting and vibration reduction. Therefore, for the first time, we investigate a metamaterial with local electromechanical resonators with nonlinearity stemming from the resonator in the present study to fill this gap. This is also motivated by our previous work that has shown the possibility of significant frequency shifts at all wavelength limits in locally resonant metamaterial with nonlinearity in the conventional mechanical resonator [45]. In this paper, we employ analytical and different numerical signal processing techniques to investigate the local and global properties of the nonlinear wave features in the proposed metamaterial. The former is demonstrated through MMS to obtain a closed-form solution for the band structure. The latter is demonstrated through investigating the spectro-spatial features of the numerical results to reveal the birth of solitary waves, existing of significant frequency shift for non-reciprocal wave propagation applications, exploring the type of wave distortion, and validating the analytical results by reconstructing the band structure. These spectro-spatial analyses include spatial wave profile, spectrograms of Short term Fast Fourier Transform (STFT), and contours of 2D Fast Fourier transform (2D FFT). Parametric analyses are also conducted to study the effect of nonlinearity and electromechanical coupling parameters on the nonlinear wave propagation features in terms of wave amplitude and harvested power. Finally, we computationally and experimentally demonstrate the presence of significant frequency shift at the long-wavelength limit in the proposed structure.

The rest of the current study is organized as follows: In Section 2, we present a mathematical model for the proposed metamaterial with nonlinear local electromechanical resonators. This is followed by the derivation of an analytical solution for the band structure. Then, we discuss the analytical findings in terms of the effect of different parameters on the bandgap size in Section 3. In Section 4, we study the spectro-spatial features of the output voltage wave by several signal processing techniques to reveal more important features of the nonlinear wave propagation phenomena in the proposed structure. Next, spectro-spatial analyses are used to validate our analytical solution in Section 5. The observed significant frequency shift is demonstrated computationally using COMSOL Multiphysics in Section 6, and experimentally in Section 7. Finally, we summarize our findings in the conclusion section.

2. Mathematical model

The proposed metamaterial with embedded nonlinear electromechanical local resonators is depicted in Fig. 1. The metamaterial consists of an infinite chain of cells with mass M . These cells are connected by a linear spring with stiffness K . A local nonlinear electromechanical resonator with an effective mass m_p is embedded in each cell. The nonlinearity in the resonator stems from a nonlinear spring with an effective linear stiffness k_1 , and cubic nonlinear stiffness $\bar{\alpha}$. A linear viscous damping is assumed in the local resonator C_2 and chain C_1 stiffness. The electromechanical local resonator is modeled as a beam sandwiched by piezoelectric layers with coupling coefficient θ and capacitance C_p . This resonator is shunted to a load resistor R , and it harvests a voltage, \bar{v}_n . If the displacement of the n th cell is defined as u_n , and the displacement of the electromechanical resonator is defined as Y_n , then the governing equations of motion for each cell with its local resonator can be written as [47,49,59]

$$M\ddot{u}_n + C_1(2\dot{u}_n - \dot{u}_{n+1} - \dot{u}_{n-1}) + K(2\bar{u}_n - \bar{u}_{n+1} - \bar{u}_{n-1}) + m_p(\ddot{y}_n + \ddot{u}_n) = 0, \quad (1)$$

$$m_p\ddot{y}_n + C_2\dot{y}_n + k_1\bar{y}_n - \theta\bar{v}_n + \bar{\alpha}\bar{y}_n^3 = -m_p\ddot{u}_n, \quad (2)$$

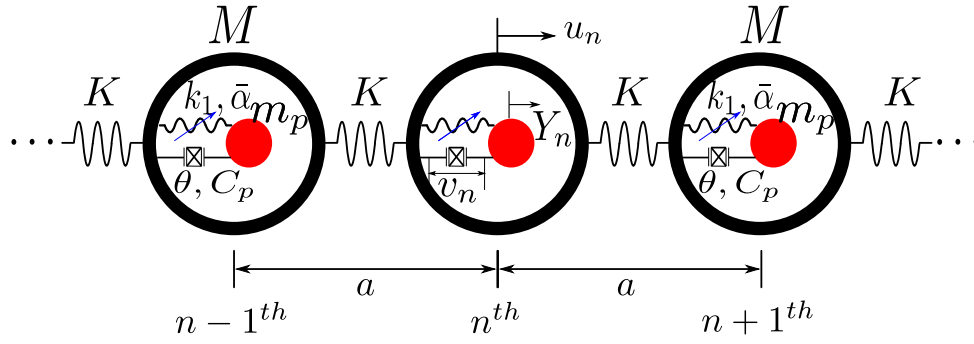


Fig. 1. A schematic for the proposed metamaterial with nonlinear local electromechanical resonators.

$$RC_p \dot{v}_n + \bar{v}_n + R\theta \dot{y}_n = 0, \quad (3)$$

where $\bar{y}_n = Y_n - \bar{u}_n$ is the relative displacement of the electromechanical resonator. The dimensionless version of these equations can be expressed as

$$\ddot{u}_n + \epsilon \mu_1 (2\dot{u}_n - \dot{u}_{n+1} - \dot{u}_{n-1}) + 2u_n - u_{n+1} - u_{n-1} + \bar{k} \Omega_0^2 (\dot{y}_n + \ddot{u}_n) = 0, \quad (4)$$

$$\Omega_0^2 \ddot{y}_n + \epsilon \mu_2 \dot{y}_n + y_n - \alpha_1 v_n + \epsilon \alpha y_n^3 = -\Omega_0^2 \ddot{u}_n, \quad (5)$$

$$\alpha_2 \dot{v}_n + v_n + \alpha_3 \dot{y}_n = 0, \quad (6)$$

where $\omega_n^2 = K/M$, $\omega_d^2 = k_1/m_p$, $\bar{k} = k_1/K$, $u_n = \bar{u}_n/U_0$, $y_n = \bar{y}_n/y_0$, $v_n = \bar{v}_n/V_0$, $\epsilon \alpha = \bar{\alpha} U_0^2/K$, $\Omega_0 = \omega_n/\omega_d$, $\epsilon \mu_1 = C_1 \omega_n/K$, $\epsilon \mu_2 = C_2 \omega_n/K$, $\alpha_1 = \theta V_0/k_1$, $\alpha_2 = RC_p \omega_n$, and $\alpha_3 = R\theta \omega_n y_0/V_0$. It is noteworthy that the dots are related to the time derivative in term of the nondimensional time, $\tau = \omega_n t$. To obtain an approximate analytical solution using MMS, we expand our solution by power series and keep only the first order terms as:

$$u_n(t, \epsilon) = u_{n0}(T_0, T_1) + \epsilon u_{n1}(T_0, T_1) + o(\epsilon^2), \quad (7)$$

$$y_n(t, \epsilon) = y_{n0}(T_0, T_1) + \epsilon y_{n1}(T_0, T_1) + o(\epsilon^2), \quad (8)$$

$$v_n(t, \epsilon) = v_{n0}(T_0, T_1) + \epsilon v_{n1}(T_0, T_1) + o(\epsilon^2). \quad (9)$$

In addition, we keep the time scales T_0 and T_1 and neglect any higher time scales at this order of perturbation where $T_0 = \tau$ is the fast time scale, and $T_1 = \epsilon \tau$ is the slow time scale. With the introduction of multiple time scales, the derivative operators will also get perturbed to

$$(\dot{}) = D_0 + \epsilon D_1 + \dots, \quad (10)$$

$$(\ddot{}) = D_0^2 + 2\epsilon D_0 D_1 + \dots, \quad (11)$$

where D_0 and D_1 denote the partial derivative with respect to the fast time scale and slow time scale, respectively. Substituting Eqs. (7)–(11) into Eqs. (4)–(6) and separating the coefficients of ϵ^0 and ϵ^1 yields order ϵ^0

$$D_0^2 u_{n0} + 2u_{n0} - u_{(n-1)0} - u_{(n+1)0} + \bar{k} \Omega_0^2 D_0^2 (y_{n0} + u_{n0}) = 0, \quad (12)$$

$$\Omega_0^2 D_0^2 y_{n0} + y_{n0} - \alpha_1 v_{n0} = -\Omega_0^2 D_0^2 u_{n0}, \quad (13)$$

$$\alpha_2 D_0 v_{n0} + v_{n0} + \alpha_3 D_0 y_{n0} = 0, \quad (14)$$

order ϵ^1

$$\begin{aligned} & D_0^2 u_{n1} + 2u_{n1} - u_{(n-1)1} - u_{(n+1)1} + \bar{k} \Omega_0^2 D_0^2 (y_{n1} + u_{n1}) \\ & = -2\bar{k} \Omega_0^2 D_0 D_1 (y_{n0} + u_{n0}) - 2D_0 D_1 u_{n0} - \mu_1 D_0 (2u_{n0} - u_{(n-1)0} - u_{(n+1)0}), \end{aligned} \quad (15)$$

$$\begin{aligned} \Omega_0^2 D_0^2 y_{n1} + y_{n1} - \alpha_1 v_{n1} = & -\Omega_0^2 D_0^2 u_{n1} - 2\Omega_0^2 D_0 D_1 u_{n0} \\ & - 2\Omega_0^2 D_0 D_1 y_{n0} - \alpha y_{n0}^3 - \mu_2 D_0 y_{n0}, \end{aligned} \quad (16)$$

$$\alpha_2 D_0 v_{n1} + v_{n1} + \alpha_3 D_0 y_{n1} = -\alpha_2 D_1 v_{n0} - \alpha_3 D_1 y_{n0}, \quad (17)$$

It can be noted from Eqs. (12)–(14) that $\mathcal{O}(\epsilon^0)$ equations are correspond to the linear equations and all the nonlinear terms appear at the equations corresponding to higher order of ϵ as excitation terms. Therefore, there will not be any difficulty to handle these equations. Having established these equations at different order of ϵ , next we present the linear dispersion relations.

2.1. Linear dispersion relations

To obtain the linear dispersion relation, the equation set at order ϵ^0 is sufficient. The solution of this set can be expressed as

$$u_n = A e^{i(nk - \omega \tau)}, \quad (18)$$

$$y_n = B e^{i(nk - \omega \tau)}, \quad (19)$$

$$v_n = C e^{i(nk - \omega \tau)}. \quad (20)$$

Substituting Eqs. (19)–(20) into Eq. (14) leads to

$$-i\alpha_2 \omega C + C - i\alpha_3 \omega B = 0. \quad (21)$$

Rearranging Eq. (21) yields

$$C = \Gamma B, \quad (22)$$

where Γ is defined as

$$\Gamma = \frac{i\alpha_3 \omega}{1 - i\alpha_2 \omega}. \quad (23)$$

Similarly, one can solve for B by introducing Eqs. (18)–(19) and Eq. (22) into Eq. (13) to get

$$B = K_\omega A, \quad (24)$$

where K_ω can be expressed as

$$K_\omega = \frac{\Omega_0^2 \omega^2}{1 - \alpha_1 \Gamma - \Omega_0^2 \omega^2}, \quad (25)$$

From Eqs. (12), (22), (24), the dispersion relation of the metamaterial with local electromechanical resonator can be written as:

$$-\omega^2 + (2 - 2 \cos k) - \bar{k} \Omega_0^2 \omega^2 (1 + K_\omega) = 0. \quad (26)$$

We emphasize that the above dispersion relation leads to 5 roots for ω with electromechanical coupling instead of 4 for the system without electromechanical coupling. Also, only 4 out of these 5 roots carry a nonzero real part.

2.2. Nonlinear dispersion relation

To obtain the approximate analytical solution (i.e., nonlinear frequency correction coefficient), we need to solve the nonlinear problem at order ϵ^1 . In particular, the solvability condition should be determined in order to guarantee the convergence of our approximate solution.

Multiplying Eq. (17) by α_1 and collecting the coefficient of v_{n1} on the left-hand side yields

$$(\alpha_2 D_0 + 1)\alpha_1 v_{n1} = \alpha_1[-\alpha_3 D_0 y_{n1} - \alpha_2 D_1 v_{n0} - \alpha_3 D_1 y_{n0}]. \tag{27}$$

To eliminate v_{n1} from Eq. (16), we multiply Eq. (16) by $(\alpha_2 D_0 + 1)$ and substitute Eq. (27). After rearrangement, Eq. (16) becomes

$$[(\alpha_2 D_0 + 1)(\Omega_0^2 D_0^2 + 1) + \alpha_1 \alpha_3 D_0] y_{n1} = -(\alpha_2 D_0 + 1)[\Omega_0^2 D_0^2 u_{n1} + 2\Omega_0^2 D_0 D_1(u_{n0} + y_{n0}) + \alpha_1 y_{n0}^3 - \mu_2 D_0 y_{n0}] - \alpha_2 \alpha_1 D_1 v_{n0} - \alpha_1 \alpha_3 D_1 y_{n0}. \tag{28}$$

To eliminate v_{n1} and y_{n1} for Eq. (15), we multiply Eq. (28) by $\bar{k}\Omega_0^2 D_0^2$ and Eq. (15) by $[(\alpha_2 D_0 + 1)(\Omega_0^2 D_0^2 + 1) + \alpha_1 \alpha_3 D_0]$, and substitute the resulting equation into Eq. (15) yields

$$\begin{aligned} & [(\Omega_0^2 D_0^2 + 1)(\alpha_2 D_0 + 1) + \alpha_1 \alpha_3 D_0]((1 + \bar{k}\Omega_0^2)D_0^2 u_{n1} + 2u_{n1} - u_{(n-1)1} \\ & - u_{(n+1)1}) - \bar{k}\Omega_0^2 D_0^2 (\alpha_2 D_0 + 1)\Omega_0^2 D_0^2 u_{n1} \\ & = [(\Omega_0^2 D_0^2 + 1)(\alpha_2 D_0 + 1) + \alpha_1 \alpha_3 D_0](-2D_0 D_1 u_{n0} - 2\bar{k}\Omega_0^2 D_0 D_1(u_{n0} + y_{n0}) \\ & - \mu_1 D_0(2u_{n0} - u_{(n-1)0} - u_{(n+1)0})) + \bar{k}\Omega_0^2 D_0^2 \\ & [- (\alpha_2 D_0 + 1)(-2\Omega_0^2 D_0 D_1(u_{n0} + y_{n0}) - \alpha_1 y_{n0}^3 - \mu_2 D_0 y_{n0}) \\ & + \alpha_1 \alpha_2 D_1 v_{n0} + \alpha_1 \alpha_3 D_1 y_{n0}]. \end{aligned} \tag{29}$$

The solvability condition can be obtained by substituting the linear solution Eqs. (18)–(20) into Eq. (29) as

$$\begin{aligned} & [(\Omega_0^2 D_0^2 + 1)(\alpha_2 D_0 + 1) + \alpha_1 \alpha_3 D_0]((1 + \bar{k}\Omega_0^2)D_0^2 u_{n1} + 2u_{n1} - u_{(n-1)1} \\ & - u_{(n+1)1}) - \bar{k}\Omega_0^2 D_0^2 (\alpha_2 D_0 + 1)\Omega_0^2 D_0^2 u_{n1} \\ & = [(-\Omega_0^2 \omega^2 + 1)(-i\alpha_2 \omega + 1) - i\alpha_1 \alpha_3 \omega](2i\omega A' + 2i\omega \bar{k}\Omega_0^2(1 + K_\omega)A' \\ & + i\mu_1 \omega A(2 - 2\cos k) - \bar{k}\Omega_0^2 \omega^2 [(i\omega \alpha_2 - 1)(2i\Omega_0^2 \omega A'(1 + K_\omega) \\ & - 3\alpha A^2 \bar{A}K_\omega^3 + i\mu_2 \omega K_\omega A) + \alpha_1 \alpha_2 K_\omega \Gamma A' + \alpha_1 \alpha_3 K_\omega A'])e^{i(nk - \omega\tau)} + \text{NST}. \end{aligned} \tag{30}$$

where NST refers to the non-secular terms.

Next, to obtain a convergent solution, the secular terms (i.e., coefficient of $e^{i(nk - \omega\tau)}$, which leads to unbounded solution) must be eliminated. Therefore, the solvability condition can then be written as

$$\begin{aligned} & [(-\Omega_0^2 \omega^2 + 1)(-i\alpha_2 \omega + 1) - i\alpha_1 \alpha_3 \omega](2i\omega A' + 2i\omega \bar{k}\Omega_0^2(1 + K_\omega)A' \\ & + i\mu_1 \omega A(2 - 2\cos k) - \bar{k}\Omega_0^2 \omega^2 [(i\omega \alpha_2 - 1)(2i\Omega_0^2 \omega A'(1 + K_\omega) \\ & - 3\alpha A^2 \bar{A}K_\omega^3 + i\mu_2 \omega K_\omega A) + \alpha_1 \alpha_2 K_\omega \Gamma A' + \alpha_1 \alpha_3 K_\omega A']) = 0. \end{aligned} \tag{31}$$

Introducing the polar form $(A = \frac{1}{2}ae^{ib}$ where a and b are real functions of T_1) and the complex values in Cartesian form (i.e., $K_\omega = \text{Re}[K_\omega] + i \text{Im}[K_\omega]$, and $\Gamma = \text{Re}[\Gamma] + i \text{Im}[\Gamma]$) in Eq. (31) leads to

$$\begin{aligned} & -ae^{ib}\alpha_2\mu_1\Omega_0^2\omega^4 + a\cos ke^{ib}\alpha_2\mu_1\Omega_0^2\omega^4 + \frac{1}{2}ae^{ib}\bar{k}(i\text{Im}[K_\omega] \\ & + \text{Re}[K_\omega])\alpha_2\mu_2\Omega_0^2\omega^4 - \alpha_2\Omega_0^2(e^{ib}a' + ae^{ib}ib')\omega^4 \\ & + \frac{3}{8}a^3e^{ib}i\alpha\bar{k}(i\text{Im}[K_\omega] + \text{Re}[K_\omega])^3\alpha_2\Omega_0^2\omega^3 - ia^{ib}\mu_1\Omega_0^2\omega^3 \\ & + a\cos ke^{ib}i\mu_1\Omega_0^2\omega^3 + \frac{1}{2}ae^{ib}i\bar{k}(i\text{Im}[K_\omega] + \text{Re}[K_\omega])\mu_2\Omega_0^2\omega^3 \\ & - i\Omega_0^2(e^{ib}a' + ae^{ib}ib')\omega^3 - \frac{3}{8}a^3e^{ib}\alpha\bar{k}(i\text{Im}[K_\omega] + \text{Re}[K_\omega])^3\Omega_0^2\omega^2 \\ & + ae^{ib}\alpha_2\mu_1\omega^2 - a\cos ke^{ib}\alpha_2\mu_1\omega^2 + ae^{ib}\alpha_1\alpha_3\mu_1\omega^2 - a\cos ke^{ib}\alpha_1\alpha_3\mu_1\omega^2 \\ & + \bar{k}\alpha_2\Omega_0^2(e^{ib}a' + ae^{ib}ib')\omega^2 + \bar{k}(i\text{Im}[K_\omega] + \text{Re}[K_\omega]) \end{aligned}$$

$$\begin{aligned} & \times \alpha_2\Omega_0^2(e^{ib}a' + ae^{ib}ib')\omega^2 - \frac{1}{2}(i\text{Im}[\Gamma] + \text{Re}[\Gamma])\bar{k}(i\text{Im}[K_\omega] + \text{Re}[K_\omega]) \\ & \times \alpha_1\alpha_2\Omega_0^2(e^{ib}a' + ae^{ib}ib')\omega^2 + \bar{k}\alpha_1\alpha_3\Omega_0^2(e^{ib}a' + ae^{ib}ib')\omega^2 \\ & + \frac{1}{2}\bar{k}(i\text{Im}[K_\omega] + \text{Re}[K_\omega])\alpha_1\alpha_3\Omega_0^2(e^{ib}a' + ae^{ib}ib')\omega^2 \\ & + \alpha_2(e^{ib}a' + ae^{ib}ib')\omega^2 + \alpha_1\alpha_3(e^{ib}a' + ae^{ib}ib')\omega^2 + ae^{ib}i\mu_1\omega \\ & - ia\cos ke^{ib}\mu_1\omega + i\bar{k}\Omega_0^2(e^{ib}a' + ae^{ib}ib')\omega + i\bar{k}(i\text{Im}[K_\omega] + \text{Re}[K_\omega]) \\ & \times \Omega_0^2(e^{ib}a' + ae^{ib}ib')\omega + i(e^{ib}a' + ae^{ib}ib')\omega = 0. \end{aligned} \tag{32}$$

Upon separating the real and imaginary parts, the following equations can be obtained

$$f + ga' + hab' = 0, \tag{33}$$

$$l - ha' + gab' = 0, \tag{34}$$

where the coefficients

$$g = -\frac{1}{2}\omega(\alpha_2\omega(\Omega_0^2(\bar{k}(\alpha_1(-\text{Im}[\Gamma])\text{Im}[K_\omega] + (\alpha_1\text{Re}[\Gamma] - 2)\text{Re}[K_\omega] - 2) + 2\omega^2) - 2) + 2\Omega_0^2\bar{k}\text{Im}[K_\omega] - \alpha_1\alpha_3\omega(\Omega_0^2\bar{k}(\text{Re}[K_\omega] + 2) + 2)), \tag{35}$$

$$h = \frac{1}{2}\omega(\Omega_0^2(\bar{k}(\text{Re}[K_\omega](\alpha_1\alpha_2\text{Im}[\Gamma]\omega - 2) + \omega\text{Im}[K_\omega](\alpha_2(\alpha_1\text{Re}[\Gamma] - 2) - \alpha_1\alpha_3) - 2) + 2\omega^2) - 2), \tag{36}$$

$$\begin{aligned} f &= \frac{1}{8}a\omega^2(\alpha_2(\omega\Omega_0^2\bar{k}(3a^2\alpha\text{Im}[K_\omega]^3 - 9a^2\alpha\text{Im}[K_\omega]\text{Re}[K_\omega]^2 \\ & + 4\mu_2\omega\text{Re}[K_\omega]) + 8\mu_1(\cos k - 1)(\omega^2\Omega_0^2 - 1)) \\ & + \Omega_0^2\bar{k}(9a^2\alpha\text{Im}[K_\omega]^2\text{Re}[K_\omega] - 3a^2\alpha\text{Re}[K_\omega]^3 - 4\mu_2\omega\text{Im}[K_\omega]) \\ & - 8\alpha_1\alpha_3\mu_1(\cos k - 1)), \end{aligned} \tag{37}$$

$$\begin{aligned} l &= \frac{1}{8}a\omega(\omega\Omega_0^2\bar{k}(3a^2\alpha\text{Im}[K_\omega]^3 + \text{Im}[K_\omega](4\alpha_2\mu_2\omega^2 - 9a^2\alpha\text{Re}[K_\omega]^2) \\ & - 9a^2\alpha\alpha_2\omega\text{Im}[K_\omega]^2\text{Re}[K_\omega] + \omega\text{Re}[K_\omega](3a^2\alpha\alpha_2\text{Re}[K_\omega]^2 + 4\mu_2)) \\ & + 8\mu_1(\cos k - 1)(\omega^2\Omega_0^2 - 1)). \end{aligned} \tag{38}$$

Among these coefficients, only l and f depends on the oscillation amplitude a . To obtain the slow-flow equations, one can solve Eqs. (33)–(34) to get

$$a' = \frac{lh - fg}{g^2 + h^2}, \tag{39}$$

$$ab' = -\frac{gl + mh}{h^2 + g^2}. \tag{40}$$

Consequently, the slow-flow equations of the system can be written as

$$a' = c_0a^3 + c_1a, \tag{41}$$

$$ab' = c_2a^3 + c_3a, \tag{42}$$

where c_0, c_1, c_2 and c_3 are constants and depend on the system parameters. It is to be noted here that these slow-flow equations are not linear functions of a . Consequently, determining the nonlinear frequency correction term for the nonlinear frequency is not straight forward. First, we will consider the case of no damping (i.e., $\mu_1 = \mu_2 = 0$). This yields $c_1 = c_3 = 0$. since the value of c_2 is significantly larger than c_0 for common energy harvester parameters, as shown in Fig. 1, one can safely assume the change in a with slow time scale T_1 is zero, which further implies $a' = 0$ and, consequently, the amplitude is constant $a = a_0$. Finally, the nonlinear frequency correction factor can be expressed as

$$b' = c_2a_0^2, \tag{43}$$

and integrating this factor with respect to the slow time scale T_1 yields

$$b = c_2 a_0^2 T_1. \quad (44)$$

On the other hand, when light linear viscous damping is considered (i.e., $\mu_1 \neq 0$ and $\mu_2 \neq 0$), the values of c_1 and c_3 are not zero anymore. Yet, the value of c_0 is still significantly smaller than the values of c_1 , c_2 , and c_3 . Therefore, one can integrate Eq. (41) as

$$a = a_0 e^{c_1 T_1}, \quad (45)$$

while

$$b' = c_2 a_0 e^{2c_1 T_1} + c_3. \quad (46)$$

It should be noted that, in the case of light damping, the wave amplitude decays slowly. Therefore, the nonlinear correction term b' is not constant and can be interpreted as an instantaneous shift in the dispersion curves.

For both cases, the nonlinear dispersion relation can be expressed as

$$\omega_{nl} = \omega - \epsilon b', \quad (47)$$

and it varies at each time instant in the case of light damping.

Next, we will consider the local stability of the wave solution. The amplitude given in Eq. (41) has either three fixed points ($a^* = 0, \pm\sqrt{-c_1/c_0}$ for $c_0 > 0$) or only one fixed point ($a^* = 0$, for $c_0 < 0$). It should be noted that c_1 is always positive. In addition, c_0 is positive for frequencies in the acoustics mode, while it is negative for frequencies in the optical modes. The local stability near each fixed point (i.e., small perturbation) can then be evaluated based on the sign of λ raising from

$$\frac{d}{da} a' |_{a^*} = 3c_0 a^{*2} + c_1 = \lambda \quad (48)$$

For the case of the acoustic mode, the system has a stable fixed point at $a^* = 0$ and two unstable fixed points at $a^* = \pm\sqrt{-c_1/c_0}$. Since we only consider small values of a in the case of weak nonlinearity, one can safely assume that the system is stable and the amplitude eventually approaches zero. This is because $c_1 \gg c_0$; therefore, $|\sqrt{-c_1/c_0}| \gg 0$, which indicates that the unstable fixed points are far away from the considered range of weak nonlinearity. On the other hand, the only fixed point in the case of the optical mode is always stable.

Since only the first order perturbation is considered in the current study, the multiple scales solution is always a stable solution for the small amplitude excitations [22].

3. Analytical bandgap parametric study

To investigate the effect of resonator's nonlinearity in the presence of electromechanical coupling on the band structure, we vary some electromechanical and nonlinear parameters (i.e., $\epsilon a a^2$, θ , and R) while other system parameters are held as constants. The fixed parameters are chosen based on [58,59] as $\bar{k} = 1$, $\omega_n = \omega_d = 100$ rad/sec, $k_1 = 10^6$ N/m, and $C_p = 13.3 \times 10^{-9}$ F. It is noteworthy that we focus on the nonlinear band structure since the discussion about the linear band structure can be found in [58]. Moreover, we validate our results in Sec. 5 by reconstructing the band structure from the 2D Fast Fourier Transform (2D-FFT). Since the effect of viscous linear damping on the band structure have been investigated in prior works [60], we will focus our attention on the effect of nonlinearity and electromechanical coupling on the band structure, which is the main contribution of the current work. Therefore, we set $\epsilon \mu_1 = \epsilon \mu_2 = 0$ in this section.

Before presenting the results, it is worthy to define the different wavelength limits. Since wavelength and wavenumber are inversely proportional to each other, the long-wavelength limit is defined at low

values of wavenumbers (i.e., $k \sim \pi/9$ in Section 4) within the first irreducible Brillouin zone (i.e., $k \in [0, \pi]$). On the other hand, the short-wavelength limit is associated with high values of wavenumbers (i.e., $k \sim 7\pi/9$ in Section 4). In addition, at a moderate value of wavenumber, we define the medium-wavelength limit (i.e., $k \sim \pi/2$ in Section 4).

The band structure of different system parameters is depicted in Fig. 2. The effect of weak nonlinearity on the band structure is demonstrated in Fig. 2(a). The results indicate that softening nonlinearity shifts the dispersion curves down while hardening nonlinearity shifts the dispersion curves up. However, this shift varies over the wavelength and the different modes. For instance, the shift is more pronounced at the short-wavelength limit in the acoustics mode. On the other hand, the shift can be observed at all wavelength limits in the optical mode with more shift at the long-wavelength limit. This observation in the shift in the optical mode at the long-wavelength limit can only be observed in the case of a nonlinear resonator, unlike the nonlinear chain case where the nonlinearity has no effect at the long-wave length limit. Since the shift is more dominant at short-/long-wavelength limits in the acoustics/optical modes, one can deduce that the effect of nonlinearity is concentrated near the resonance frequency of the nonlinear electromechanical local resonator and degrades gradually with mistuning.

For typical weak electromechanical coupling ($\theta = 10^{-10}$ N/m), the electromechanical coupling has no effect (i.e., altering the band structure or the size of bandgap) on the band structure as demonstrated in Fig. 2(b). This indicates that the proposed metamaterial can be employed for simultaneous energy harvesting and vibration reduction applications. However, the attenuation level inside the bandgap is degraded due to this coupling [58]. On the other hand, the band structure of the system changed significantly at very strong electromechanical coupling (i.e., $\theta \geq 10^{-2}$) as shown in Fig. 2(c). In particular, the acoustics and optical modes start merging into one dispersion curve with increase in the electromechanical coupling. Moreover, some real frequencies appear at frequencies higher than the optical mode range in the absence of the electromechanical coupling. The strong electromechanical coupling also affects the attenuation level inside the bandgap significantly, as shown in Fig. 2(d). Also, the attenuation at higher frequencies increases with increasing electromechanical coupling as both mode merges into one dispersion curve. Although with strong mechanical coupling the dispersion curves merge into one dispersion curve, the effect depends significantly on the shunted resistor. For instance, the dispersion curves gradually merge into one dispersion curve as the resistor increases for electromechanical coupling of $\theta = 10^{-1}$ N/V, as shown in Fig. 2(e). In addition, the resistor affects the attenuation level inside the bandgap frequencies. At higher frequencies in the presence of strong electromechanical coupling, increasing the resistor's value leads to reducing the range of the wavenumber's values. Consequently, we observe a reduction in the attenuation level inside the bandgap frequencies, as shown in Fig. 2(f). To elaborate this further, exciting the system by a wave with a frequency within the bandgap leads to complex values of wavenumbers. Substituting these complex values in Eq. (18) will produce an exponentially decaying component that prevents the wave from propagating through the structure. This decay (the attenuation level) increases with increasing values of wavenumber. Therefore, reducing the values of wavenumber with increasing the shunted resistor reduces the attenuation level inside the bandgap [61], as depicted in Figs. 2 (d) and (f).

4. Spectro-spatial analyses

The obtained analytical solutions are useful in determining the effect of nonlinearity on dispersion curves and obtaining the cut off frequency (i.e., the limit of acoustics/optical modes frequencies). However, it fails to get other important characteristics of the propagating nonlinear waves. Therefore, we conduct spectro-spatial analyses to

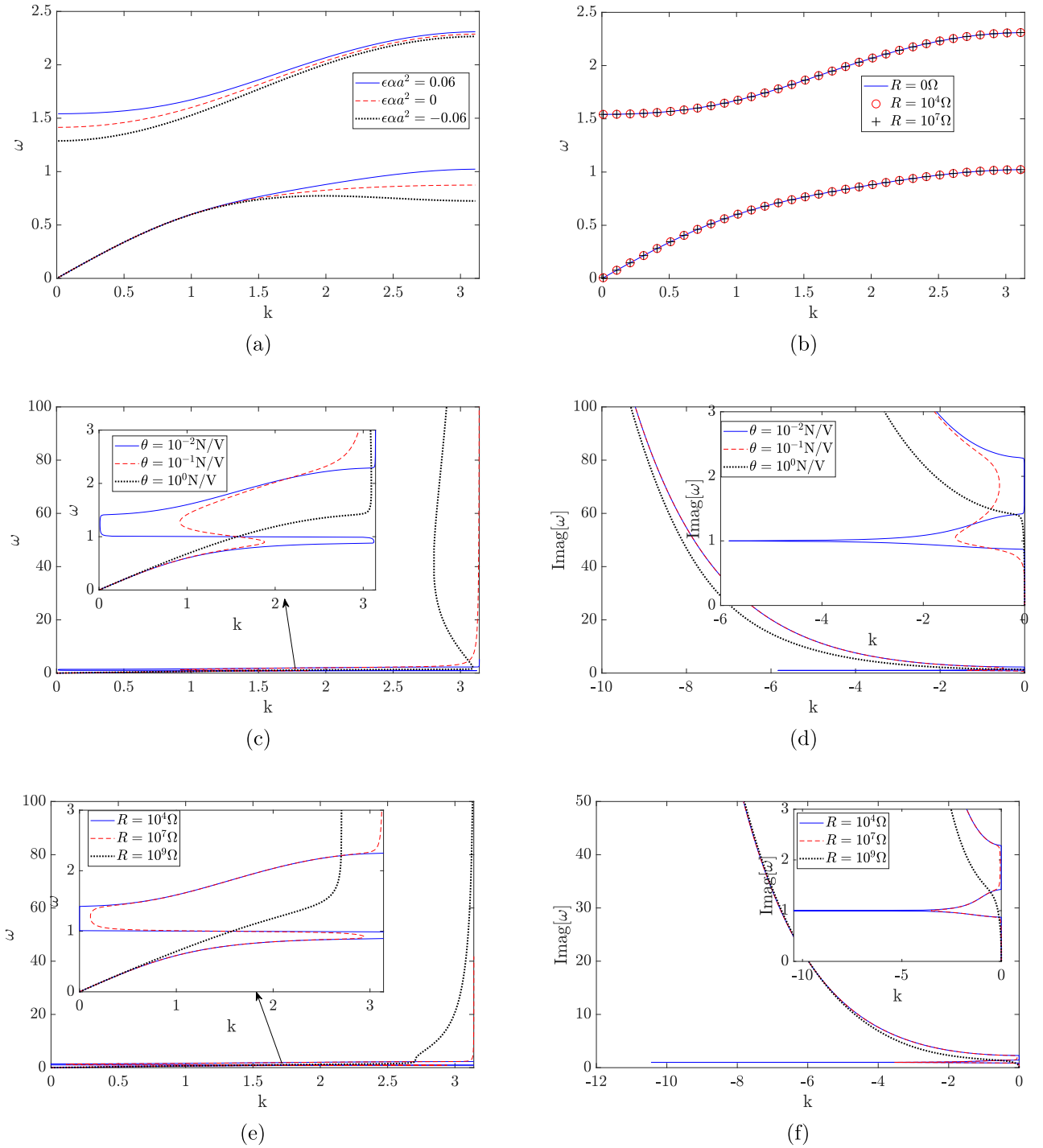


Fig. 2. Effect of different parameters on the system band structure: (a) The effect of nonlinearity without electromechanical coupling; (b) The effect of weak electromechanical coupling with hardening nonlinearity, $\theta = 10^{-10}$ N/V; (c) The effect of strong coupling with hardening nonlinearity (real), $R = 10^7 \Omega$; (d) The effect of strong coupling with hardening nonlinearity (imaginary), $R = 10^7 \Omega$; (e) The effect of resistor with strong coupling with hardening nonlinearity (real), $\theta = 10^{-1}$ N/V; (f) The effect of resistor with strong coupling with hardening nonlinearity (imaginary), $\theta = 10^{-1}$ N/V.

reveal more interesting features of the nonlinear waves that propagate through a metamaterial with nonlinear electromechanical resonator. In the present study, we focus our analyses on the harvested voltage from the nonlinear harvester. We numerically integrate a chain with 500 cells with the same parameters defined in the previous section. The chain is initially subjected to transient wave packets defined by the following set of equations

$$u_m(0) = \frac{1}{2}(H(m-1) - H(m-1 - N_{cy}2\pi/k))(1 - \cos(mk/N_{cy})) \sin(mk), \quad (49)$$

$$\begin{aligned} \dot{u}_m(0) = & \frac{1}{2}(H(m-1) \\ & - H(m-1 - N_{cy}2\pi/k))(-\omega_n\omega/N_{cy} \sin(mk/N_{cy}) \sin(mk) \\ & - \omega_n\omega(1 - \cos(mk/N_{cy})) \cos(mk)), \end{aligned} \quad (50)$$

$$y_m(0) = K_\omega u_m(0), \quad (51)$$

$$\dot{y}_m(0) = K_\omega \dot{u}_m(0), \quad (52)$$

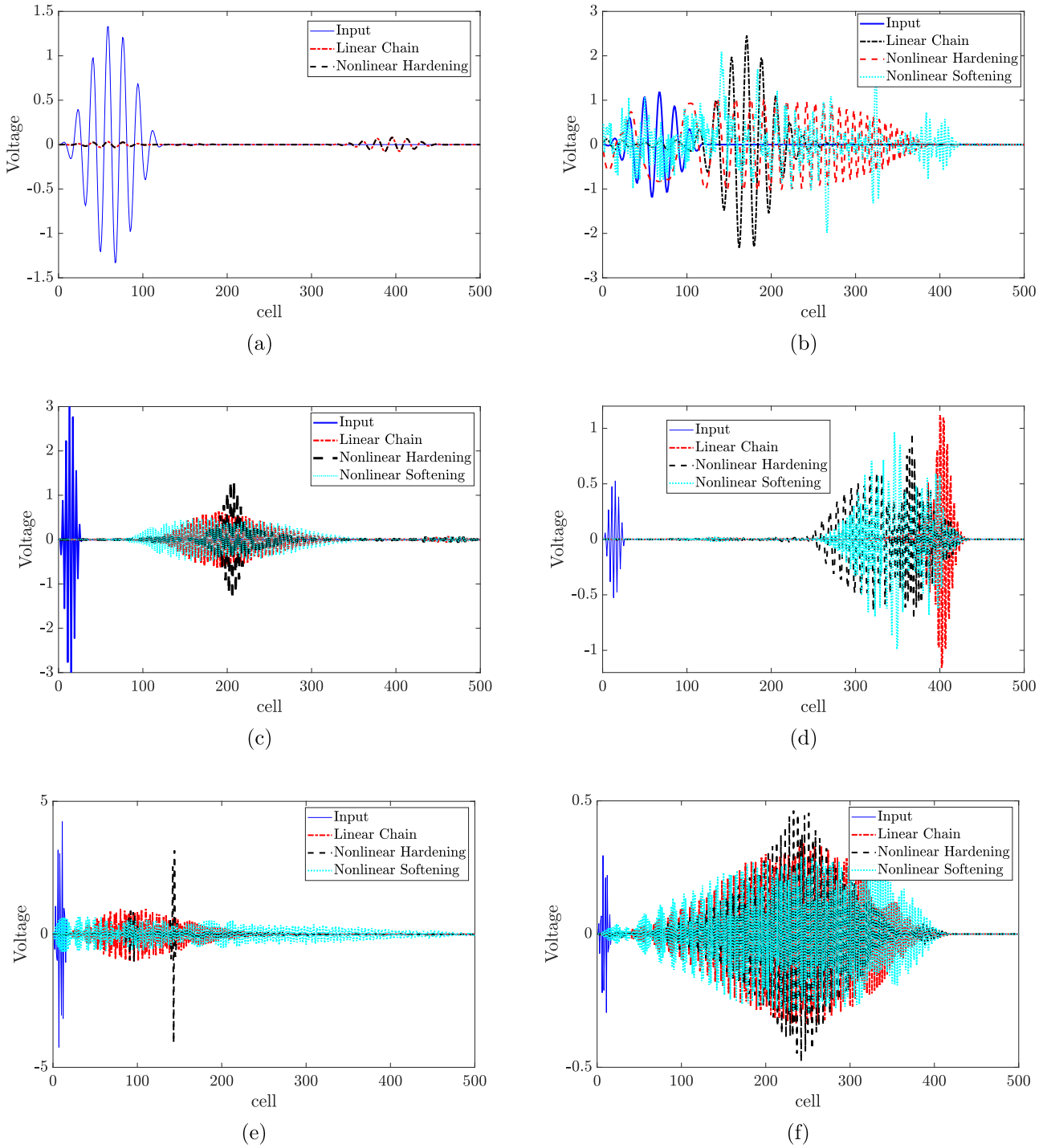


Fig. 3. Spatial profile of output voltage, $R = 10^7 \Omega$, $\theta = 10^{-8} \text{ N/V}$, $\epsilon\mu_1 = \epsilon\mu_2 = 0$: (a) Acoustics mode $k = \pi/9$; (b) Optical mode $k = \pi/9$; (c) Acoustics mode $k = \pi/2$; (d) Optical mode $k = \pi/2$; (e) Acoustics mode $k = 7\pi/9$; (f) Optical mode $k = 7\pi/9$.

$$v_m(0) = \Gamma K_\omega u_m(0), \quad (53)$$

where the subscript m denotes the initial condition of the m th cell, N_{cy} is the number of cycles and it is set to 7 in the present study, and $H(x)$ is the Heaviside function.

4.1. Spatial profile of propagating waves

In this subsection, we investigate the output voltage spatial wave profile for different types of nonlinearities and at different wavelength

limits, as depicted in Fig. 3. At the long-wavelength limit in the acoustics mode, the results indicate that the harvested voltage wave is not distorted by the nonlinearity (i.e., output wave has the same profile in the linear and nonlinear chains) as shown in Fig. 3(a). Moreover, the output wave has a low amplitude since the excitation frequency is away from the resonance frequency of the local resonator/harvester. On the other hand, the wave gets severely distorted due to nonlinearity at the long-wavelength limit in the optical mode, as shown in Fig. 3(b). For linear metamaterial, the wave is not distorted at all, although its amplitude gets amplified because the excitation frequency is close to the local resonator/harvester frequency. However, nonlinearity in

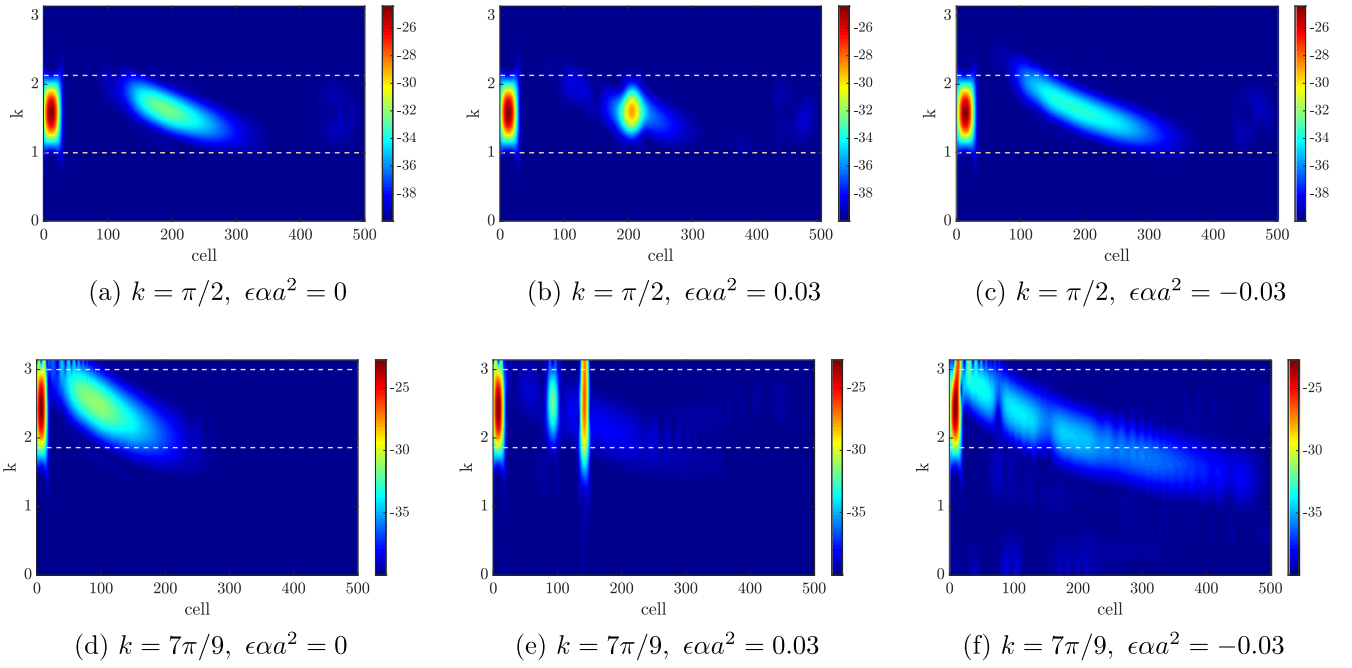


Fig. 4. Spectrograms of the STFT for the output voltage in the acoustics mode $R = 10^7 \Omega$, $\theta = 10^{-8} \text{ N/V}$, $\epsilon\mu_1 = \epsilon\mu_2 = 0$: (a) Linear chain in the medium-wavelength limit, the output wave is dispersive; (b) Hardening nonlinear chain in the medium-wavelength limit, the output wave is localized; (c) Softening nonlinear chain in the medium-wavelength limit, the output wave is dispersive; (d) Linear chain in the short-wavelength limit, the output wave is dispersive; (e) Hardening nonlinear chain in the short-wavelength limit, the output wave is localized; (f) Softening nonlinear chain in the short-wavelength limit, the output wave is dispersive.

the local resonator leads to a significant wave distortion for both, softening and hardening nonlinearities. This distortion leads to a significantly frequency conversion, as we will show in the following sections. This observation raises attraction to metamaterial with nonlinear electromechanical harvester due to the achieved wave distortion at the long-wavelength limit which cannot be obtained by other nonlinear systems like the nonlinear chain [44]. Indeed, this wave distortion can lead to a significant frequency shift (as we will show in the subsequent sections) and thus enabling the design of mechanical or electromechanical diodes that can be operated at the long-wavelength limit. Although the harvested power by the nonlinear resonator is slightly lower than the harvested power by the linear resonator case, the amplitude of the nonlinear wave has a level similar to that of the input signal.

At medium-wavelength limit in the acoustics mode (see Fig. 3(c)), the output wave becomes dispersive (i.e., stretched over the cells with lower amplitude) for the linear local resonator case since the dispersion curve at this wavelength limit has a variable slope [62]. However, nonlinearity in the resonator results in distorting the output wave. This distortion appears as an increase in the amplitude due to hardening nonlinearity. Indeed, the wave has one dispersive component with low amplitude and one traveling localized amplitude with high amplitude, unlike the linear wave, where it has only one dispersive component. In addition, the wave becomes more dispersive in the case of softening nonlinearity. This distorted wave is even more dispersive than the linear wave in terms of lower amplitude and stretches more over the chain. In the optical mode (see Fig. 3(d)), the nonlinearity distorts the wave in mainly three components for both hardening and softening nonlinearity, unlike the linear case, which has only one component. It is noteworthy that the linear output voltage waves appear to have amplitude higher than the input amplitude in the presence of the energy harvester; however, the linear wave that propagates through the chain is usually dispersive at this wavelength limit and has amplitude lower than the input signal in the absence of the energy harvester [45].

At short-wavelength limit in the acoustics mode (see Fig. 3(e)), the effect of nonlinearity becomes more pronounced in terms of stretching the linear dispersive wave further due to the softening nonlinearity or the developed localized amplitude due to the hardening nonlinearity as

compared to the medium-wavelength limit in Fig. 3(c). Moreover, one can also observe another traveling localized component with amplitude lower than the main localized component and higher than the dispersive component. However, Fig. 3(f) demonstrates that this effect is not that significant in the optical mode at the same wavelength limit since the resonance frequency of the nonlinear resonator is away from this region [45]. Nevertheless, the wave is still more dispersive with lower amplitude in the case of softening nonlinearity while it has traveling localized high amplitude component in the case of the hardening chain.

4.2. Images of STFT of the propagating waves

In order to reveal more important characteristics of the propagating voltage wave through the proposed metamaterial, we monitor the change of the output voltage wave features over the spatial domain by determining the STFT of the signal. Then, we plot the spectrograms of the resulted signal after the processing, and the input signal with applying a Hann window with the size of the input burst. The window is applied to confine the short spatial components over the space. This window is highlighted on the spectrograms between two horizontal dashed lines.

For signals in the acoustics mode, we plot the spectrograms in Fig. 4. Since the nonlinearity has no effect on the output wave at long-wavelength limit in this mode, we did not show the spectrograms of this signal. At medium-wavelength limit, the output voltage wave is dispersive in the linear metamaterial, as shown in Fig. 4(a). Thus, the output wave has an amplitude significantly lower than the input signal and is stretched over the chain. However, the output signal has only one component. In the presence of the hardening nonlinearity Fig. 4(b), the wave becomes severely distorted and is split into two components; one is localized and contains most of the energy content, and the other is stretched and has low energy content. On the contrary, the softening nonlinearity stretches the output wave further, as shown in Fig. 4(c). The energy content of this wave is distributed over only one component. Furthermore, some of the energy content appears outside the Hann window that contains the input signal, indicating that the severity of the distortion resulted from the softening nonlinearity. For

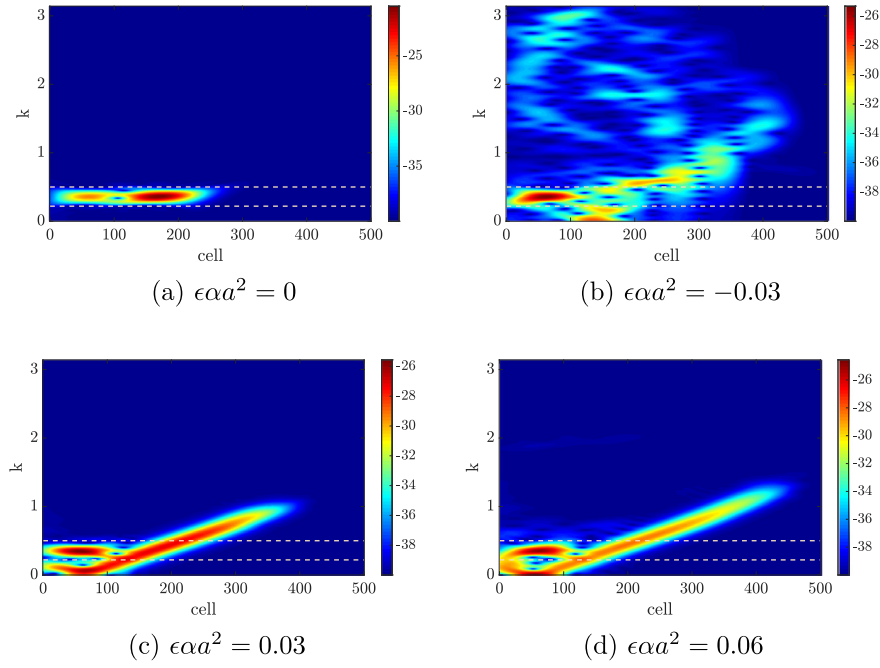


Fig. 5. Spectrograms of the STFT for the output voltage at the long-wavelength limit in the optical mode $k = \pi/9$, $R = 10^7 \Omega$, $\theta = 10^{-8} \text{ N/V}$, $\epsilon\mu_1 = \epsilon\mu_2 = 0$: (a) Linear case, no wave distortion; (b) Softening nonlinearity, significant wavenumber/frequency shift; (c) Hardening nonlinearity, significant wavenumber/frequency; (d) Stronger hardening nonlinearity, significant wavenumber/frequency.

signals at a short-wavelength limit in the acoustics mode, the results indicate that the output voltage wave in the linear case has energy content higher than that at medium-wavelength limit, as shown in Fig. 4(c). This is because the excitation frequency is closer to the local electromechanical resonator frequency in the short-wavelength limit case. This energy is confined within one component and stretches over the chain more severely than the case of medium-wavelength limit. As of the case of the medium-wavelength limit, similar distortion is observed at the short-wavelength limit for hardening and softening nonlinearities, as shown in Fig. 4(d)–(f). However, this distortion is more severe at the short-wavelength limit. For instance, unlike the case of linear chain Fig. 4(d), the hardening nonlinearity splits the output wave into three components (see Fig. 4(e)); the first is localized and contains most of the energy content (solitary wave), the second is dispersive (stretched over the cells) and has very low energy content, and the third is also localized with medium energy content. Although the latter can be observed at small values of resonator nonlinearity, it can only be observed at large values of nonlinearity in the case of the nonlinear chain [58] where a unique solitary wave is developed. On the contrary, the softening nonlinearity stretches the output voltage wave further over the chain (i.e., as compared to the linear case at the medium and short-wavelength limits and softening nonlinear case at medium-wavelength limit), as shown in Fig. 4(f). This stretch results in significant output wave energy content out on the window of the input signal.

We plot the spectrograms at the long-wavelength limit of the optical mode in Fig. 5. We focus on this region since one of the interesting characteristics of the proposed metamaterial is to realize severe distortion and significant frequency shift of the output signal by the nonlinearity in this region. For the linear case (see Fig. 5(a)), although the output voltage wave is amplified due to the tuning between the excitation frequency and the resonance frequency of the local resonator, the wave is not distorted since it is completely confined within the window of the input signal. However, the presence of nonlinearity in the local resonator distorts the output wave significantly. For instance, softening nonlinearity splits the wave into multiple components with different energy content distribution, as shown in Fig. 5(b). Most of these components lie outside the Hann window of the input signal. This indicates

that a significant frequency/wavenumber shift can be obtained by softening nonlinearity in the local resonator at the long-wavelength limit. Hardening nonlinearity also results in severe wave distortion at the long-wavelength limit, as shown in Figs. 5 (c) and (d). The results demonstrate that the output signal is stretched over a wide range of frequency/wavenumber and distributed mainly within two main components. The energy content of these components is distributed almost equally with high energy content in both components. It is noteworthy that the energy content of components in the case of hardening nonlinearity is higher than the case of softening nonlinearity. Increasing the nonlinearity (see Fig. 5(d)) results in stretching (distorting) the output voltage wave further; however, the energy content becomes lower. The observed significant frequency shift at the long-wavelength limit in the optical mode indicates that the proposed system can be used in designing electromechanical diode. This interesting frequency conversion cannot be achieved by nonlinearities stemming from the stiffness between the chain's cells [44,58].

Furthermore, we study the effect of nonlinearity on the output voltage wave at medium and short-wavelength limits in the optical mode. The spectrograms of these cases are depicted in Fig. 6. At medium-wavelength limit, we observe that the wave is not distorted in the linear case, and its component lies completely inside the window of the input signal, as shown in Fig. 6(a). However, nonlinearity of the local resonator results in a severe wave distortion; thus the emergence of a significant frequency/wavenumber shift, as shown in Figs. 6 (b) and (c). Moreover, nonlinearity splits the output wave into three main components; one is completely inside the window of the input signal with low energy content, and two outside this window. One of those two components having most of the energy content is observed above/below the input frequency range in the case of hardening/softening nonlinearity while the other has low energy content, but it is still higher than the energy content of the first component inside the window. This component lies below/above the window in the case of hardening/softening nonlinearity. The significant frequency shift at this wavelength limit (i.e., medium-wavelength limit) demonstrates that the proposed metamaterial can also be used to design an electromechanical diode that operates within the medium-wavelength limit. Therefore, the proposed structure can be used at the long and medium-wavelength limits, unlike

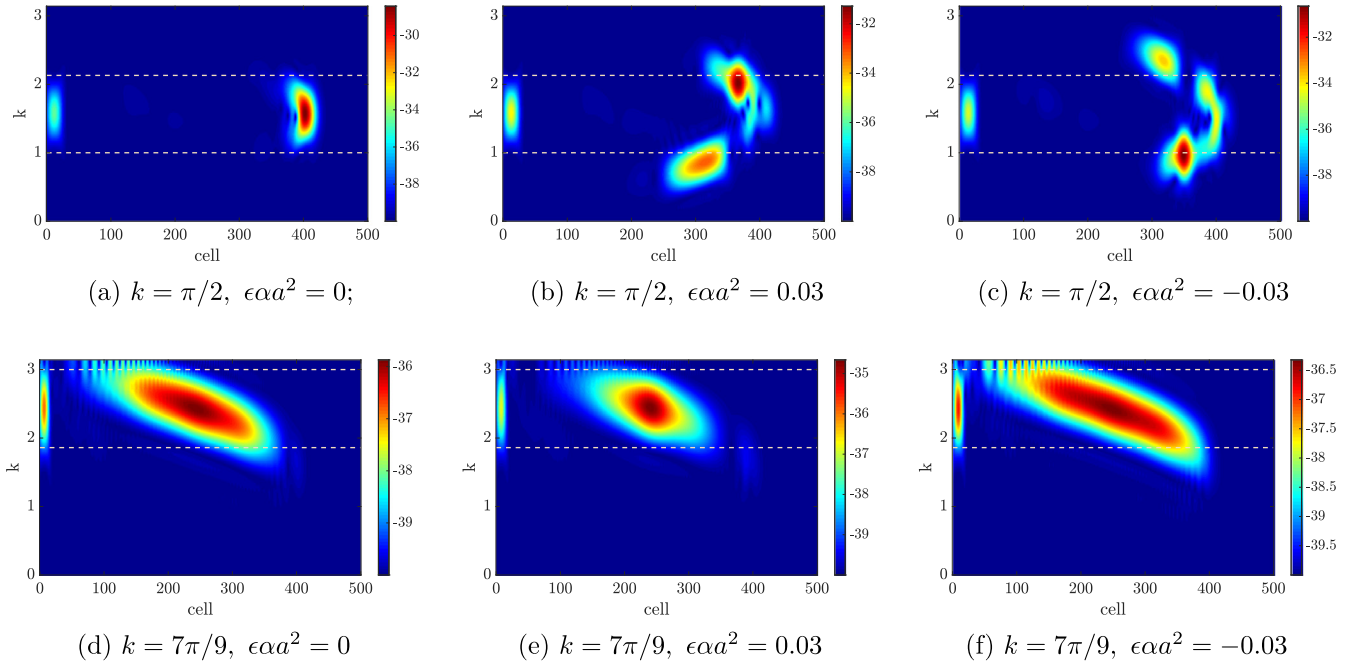


Fig. 6. Spectrograms of the STFT for the output voltage in the optical mode $R = 10^7 \Omega$, $\theta = 10^{-8} \text{ N/V}$, $\epsilon\mu_1 = \epsilon\mu_2 = 0$: (a) Linear chain in the medium-wavelength limit, no significant wavenumber/frequency shift; (b) Hardening nonlinear chain in the medium-wavelength limit, significant wavenumber/frequency shift; (c) Softening nonlinear chain in the medium-wavelength limit, significant wavenumber/frequency shift; (d) Linear chain in the short-wavelength limit, the output wave is dispersive; (e) Hardening nonlinear chain in the short-wavelength limit, the output wave is localized; (f) Softening nonlinear chain in the short-wavelength limit, the output wave is dispersive.

the case of nonlinear chain where it can only be utilized at medium-wavelength limit. At the short-wavelength limit in the optical mode, the output voltage wave is stretched over the chain in the linear case, as depicted in Fig. 6 (d). Indeed, the wave is dispersive, although it has a high amplitude resulting from frequency tuning. The effect of the nonlinearity at this wavelength limit appears as localizing the wave in the case of hardening nonlinearity (see Fig. 6(e)), and further stretching of the output signal in the case of the softening nonlinearity (see Fig. 6(f)). However, this effect is not significant (i.e., as compared to the results at the same wavelength in the acoustics mode) since the frequency in this region is away from the resonance frequency of the nonlinear local electromechanical resonator [45].

Finally, we consider the effect of damping on the observed frequency shift at the long-wavelength limit. To demonstrate that, we plot in Fig. 7 the STFT for different values of damping for each type of nonlinearity (i.e., hardening and softening). For hardening nonlinearity (Figs. 7(a)–(c)), the results indicate that metamaterials with light damping can still show significant frequency shift since some of the energy content appears outside the window of the input frequency, as depicted in Fig. 7(b). However, the energy content in the presence of damping is lower (as compared to the case of no damping shown in Fig. 7(a)) since the wave's amplitude decays over the chain and the wave is evanescent. Increasing the damping further results in faster decaying in the wave amplitude along the chain. Therefore, the output wave does not have a significant energy content at the output cell, as shown in Fig. 7(c). Similar observations can be deduced in the case of softening nonlinearity (Figs. 7(d)–(f)). In particular, significant frequency shift can be observed in the case of light damping (Fig. 7(e)), while the wave decays rapidly at higher values of damping (Fig. 7(f)).

4.3. Contour plots of 2D FFT of the propagating wave

In order to reconstruct the band structure, demonstrate the role of nonlinearity on the dispersion curves, demonstrate the frequency shift further, and investigate the birth of solitary waves, we plot the contour plots of 2D FFT of the propagating wave in Figs. 8–10.

For the acoustics mode, we only show the results at short and medium-wavelength limits since the nonlinearity has no effect at the long-wavelength limit in this mode. For the linear case at the medium-wavelength limit (see Fig. 8(a)), the contour plot indicates that the dispersion curve has a non-constant slope (nonlinear curve), and thus the wave is dispersive [62]. Hardening nonlinearity changes the dispersion curve significantly and makes its slope almost constant (linear curve), as shown in Fig. 8(b). This indicates the birth of solitary wave due to hardening nonlinearity [62]. On the other hand, softening nonlinearity bends the dispersion curve further to make the slope more nonlinear; therefore, the resulting wave is more dispersive, as depicted in Fig. 8(c). At the short-wavelength limit in the acoustics mode, the contour plot of the linear case indicates that the dispersion curves have a variable slope (nonlinear curve), and the wave is dispersive, as shown in Fig. 8(d). However, the bend is more pronounced in this case as compared to the medium-wavelength limit case, and thus the curve is more nonlinear and the stretch of this wave is more severe. Fig. 8(e) presents the contour plots in the case of hardening nonlinearity. The results demonstrate the birth of solitary localized wave due to bending the curve toward fixed slope curve. Moreover, the results indicate the birth of another solitary wave below the main solitary localized wave with lower energy content. Fig. 8(f) shows the contour plot in the case of softening nonlinearity. It can be deduced that softening nonlinearity bends the dispersion curve to become more nonlinear (variable slope), and thus the output wave is more stretched over the chain. It is noteworthy that although the effect of nonlinearity at short-wavelength limit is similar to the effect at medium-wavelength limit, the effect in the case of short-wavelength limit is more severe. This can also be deduced from the analytical results in the previous section and can be explained by the closeness of the frequencies within short-wavelength limit from the resonance frequency of the nonlinear local resonator.

Unlike the acoustics mode, the nonlinearity distorts the output wave at the long-wavelength limit in the optical mode. We present the contour plots of 2D FFT at small wavenumbers (i.e., long-wavelength limit) in the optical mode in Fig. 9. Fig. 9(a) shows the contour plot for the linear case. The results indicate that the energy of the contour plot is concentrated within the frequency of the input signal. Therefore,

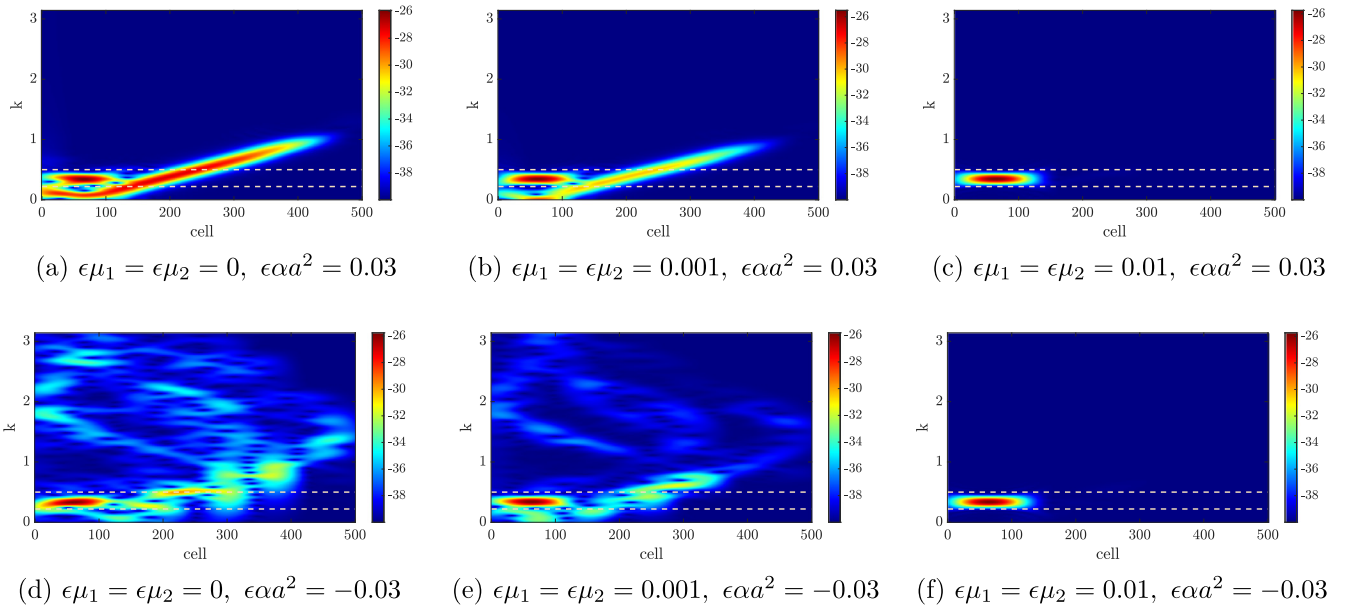


Fig. 7. Spectrograms of the STFT for the output voltage in the optical mode $R = 10^7 \Omega$, $\theta = 10^{-8} \text{ N/V}$: Hardening nonlinearity in (a) $\epsilon\mu_1 = \epsilon\mu_2 = 0$; (b) $\epsilon\mu_1 = \epsilon\mu_2 = 0.001$; (c) $\epsilon\mu_1 = \epsilon\mu_2 = 0.01$; and softening nonlinearity in (d) $\epsilon\mu_1 = \epsilon\mu_2 = 0$; (e) $\epsilon\mu_1 = \epsilon\mu_2 = 0.001$; (f) $\epsilon\mu_1 = \epsilon\mu_2 = 0.01$.

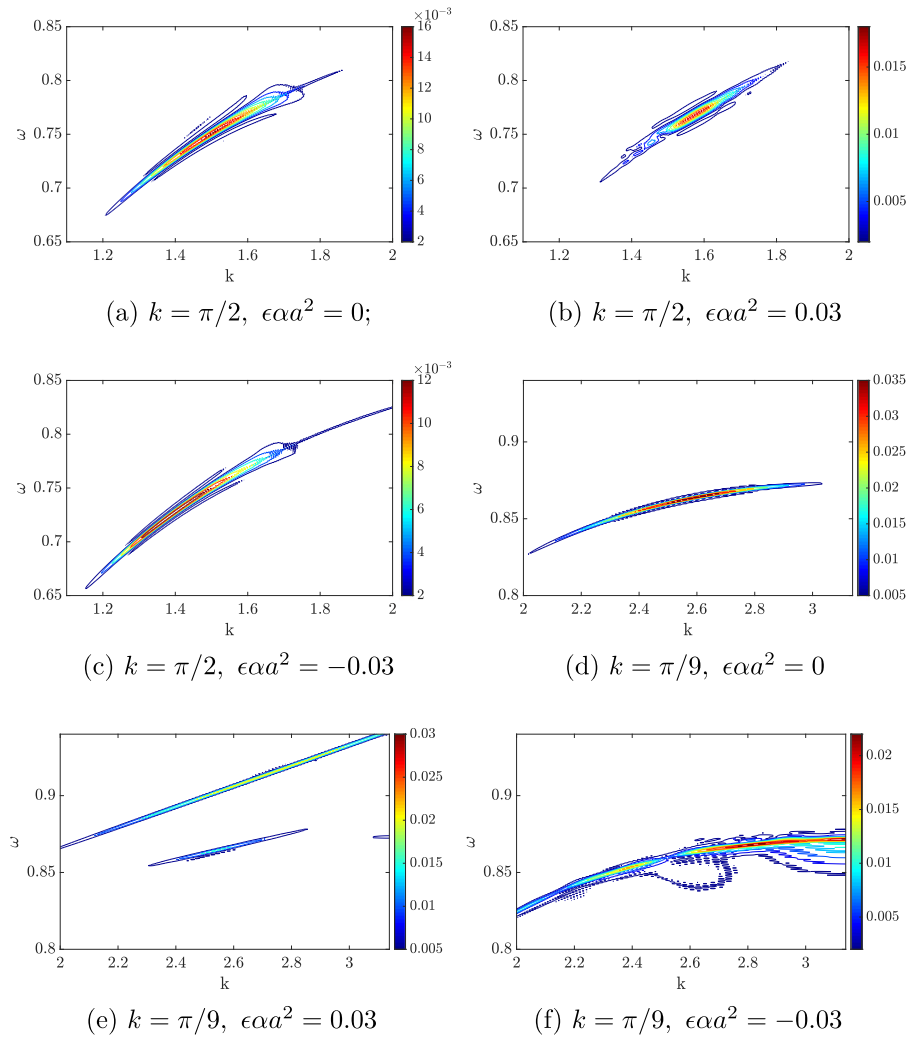


Fig. 8. Contour plots of the 2D FFT for the output voltage in the acoustics mode $R = 10^7 \Omega$, $\theta = 10^{-8} \text{ N/V}$, $\epsilon\mu_1 = \epsilon\mu_2 = 0$: (a) Medium-wavelength limit, linear case; (b) Medium-wavelength limit, hardening nonlinearity; (c) Medium-wavelength limit, softening nonlinearity; (d) Short-wavelength limit, linear case; (e) Short-wavelength limit, hardening nonlinearity; (f) Short-wavelength limit, Softening nonlinearity.

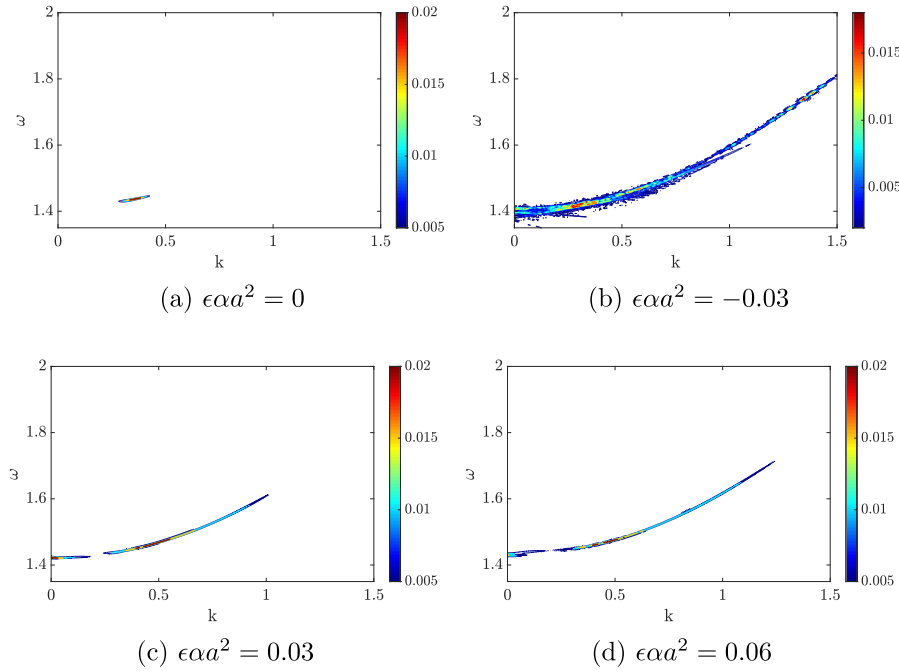


Fig. 9. Contour plots of the 2D FFT for the output voltage at the long-wavelength limit in the optical mode $k = \pi/9$, $R = 10^7 \Omega$, $\theta = 10^{-8} \text{ N/V}$, $\epsilon\mu_1 = \epsilon\mu_2 = 0$: (a) Linear case, no wave distortion; (b) Softening nonlinearity, significant wavenumber/frequency shift; (c) Hardening nonlinearity, significant wavenumber/frequency; (d) Stronger hardening nonlinearity, significant wavenumber/frequency.

no wave distortion is observed in the linear case. However, softening nonlinearity results in sever distortion since the energy content in the contour plot of the signal appears over a wide range of frequencies other than the input excitation frequency (i.e., appears at wide portion of the dispersion curve) as plotted in Fig. 9(b). Moreover, hardening nonlinearity results also in significant frequency conversion at this wavelength limit. For instance, the results in Fig. 9(c) show that the corresponding dispersion curve is stretched over wide range of frequencies. Therefore, the propagating wave appears at frequencies different than the input frequency. The effect of increasing nonlinearity on the contour plots is shown in Fig. 9(d). The results indicate that increasing the nonlinearity increases the stretch of frequency component over a wider range of frequencies.

Next, we show the contour plots of 2D FFT at medium and short-wavelength limits in the optical mode. Fig. 10(a) show the contour plot of the linear case at medium-wavelength limit. The results indicate that the frequency content of the contour plot is concentrated around the input frequency. Therefore, no frequency shift is observed in the linear case. However, hardening nonlinearity in the local resonator results in significant frequency shift since the energy of the contour plots is mainly concentrated in three regions as shown in Fig. 10(b). This is not surprising since we have already observed these three component in Fig. 6(b). Two of these regions appear away from the original frequency of the input signal and have energy content higher than the energy content of the component within the input frequency range. Moreover, the upper component has a fixed slope; therefore, it represents a localized (solitary) wave. Similar frequency shift is also observed in the case of softening nonlinearity as shown in Fig. 10(c). The energy content is also split into three components; however, the component of most energy content exists near the the lowest point of the dispersion curve unlike the case of hardening nonlinearity. For waves at short wave length limit, the contour plots of the linear case (depicted in Fig. 10(d)) demonstrate that the dispersion curve has a variable slope. Therefore, the wave is dispersive and stretched over the chain. Since this frequency region is away from the resonance frequency of the local electromechanical resonator, the effect of nonlinearity is not significant in this region as compared to the short-wavelength limit in the acoustics mode. Yet, the slight effect appears as localizing the energy component

in the case of hardening nonlinearity (Fig. 10(e)) and stretching the energy component over the dispersion curve (i.e., the output signal has frequency components other than the input signal frequency) in the case of softening nonlinearity as shown in Fig. 10(f).

5. Analytical results validation using reconstructed dispersion curves from 2D FFT of the numerical results

In the previous section, we have shown that nonlinear dispersion curves can be reconstructed from the contour plots of 2D FFT of the numerical results. In this section, the numerical dispersion curves are used to check the validity of the obtained analytical solution and ascertain its limitation. At short-wavelength limit in the acoustics mode, the analytical results indicate that the effect of nonlinearity is the highest in this mode. The contour plot in this region indicates that the analytical results can predict the cut-off frequency for $\epsilon\alpha^2 \leq 0.03$, as shown in Fig. 11(a). In particular, the main solitary wave (which has most of the energy content) is almost confined within the analytical nonlinear dispersion curve. It is noteworthy that the dispersive component of the signal (which has low energy content) coincides with the linear dispersion curve. The error becomes more significant with increasing nonlinearity and our analytical solution fails to predict the cut-off frequency in this region with stronger nonlinearity, as depicted in Fig. 11(b). For better prediction of the cut-off frequency, higher order perturbation should be considered. The analytical results also indicate that the effect of nonlinearity is more pronounced at long-wavelength limit in the optical mode. In this region, our approximate solution also fails to predict the exact cut-on frequency, as shown in Figs. 11 (c) and (d). This can be explained by the significant frequency shift observed at the long-wavelength limit discussed in the previous sections. In the short-wavelength limit in the optical mode, the analytical results slightly overestimate the cut-off frequency, as shown in Figs. 11 (e) and (f). This error increases with increasing nonlinearity although the effect of nonlinearity is minimal at this wavelength limit in the optical mode as demonstrated in the analytical and spectro-spatial results. It is noteworthy that although our analytical solution fails to predict the exact cut-off frequencies at some regions, it can provide an insights about the regions most affected by nonlinearity. This conclusion was

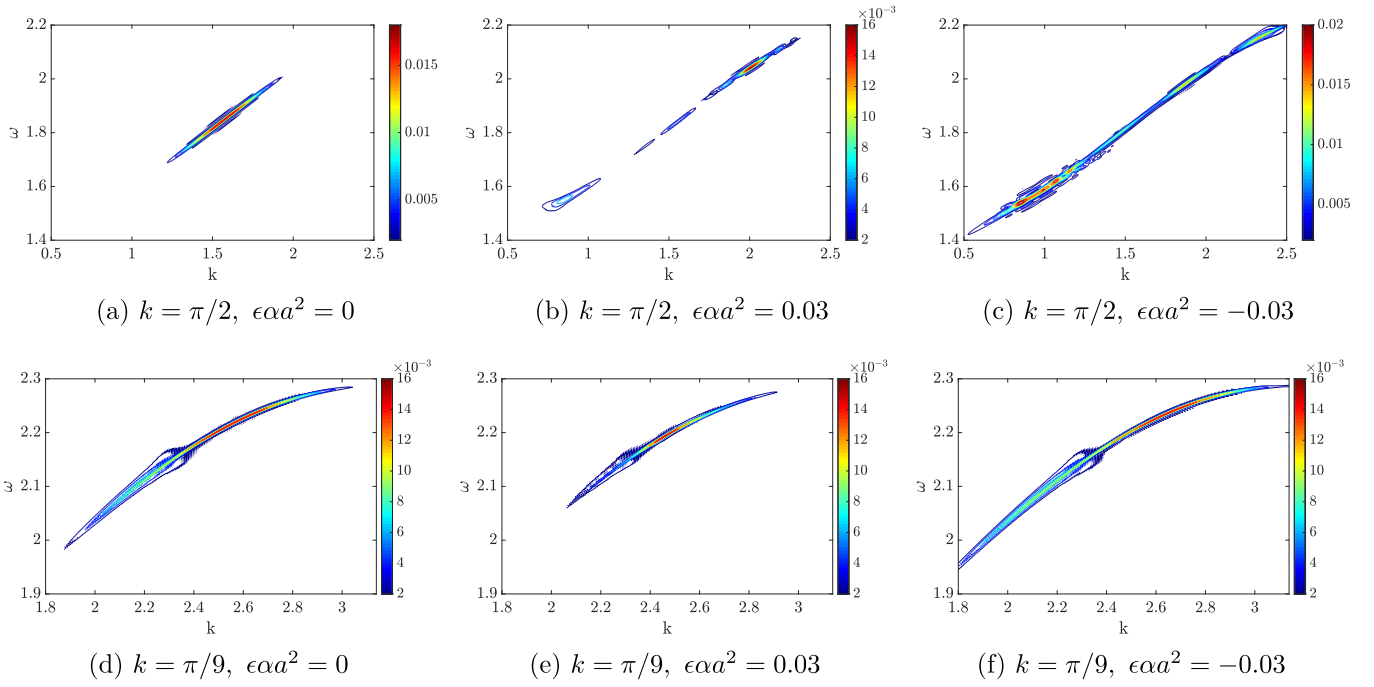


Fig. 10. Contour plots of the 2D FFT for the output voltage in the optical mode $R = 10^7 \Omega$, $\theta = 10^{-8} \text{ N/V}$, $\epsilon\mu_1 = \epsilon\mu_2 = 0$: (a) Medium-wavelength limit, linear case; (b) Medium-wavelength limit, hardening nonlinearity; (c) Medium-wavelength limit, softening nonlinearity; (d) Short-wavelength limit, linear case; (e) Short-wavelength limit, hardening nonlinearity; (f) Short-wavelength limit, Softening nonlinearity.

supported by the spectro-spatial analyses discussed in the previous section. For instance, the analytical results show that the effect of nonlinearity is more pronounced at the long-wavelength limit in the optical mode. Similarly, the spectro-spatial analyses of the numerical results demonstrated that the effect of nonlinearity in this region is the most significant due to the severe wave distortion.

6. Computational demonstration of significant frequency shift using COMSOL multiphysics

In order to further demonstrate the significant frequency shift observed at the long-wavelength limit, we simulate a nonlinear periodic structure using COMSOL Multiphysics. We followed [63] in modeling our nonlinear structure; we model our resonator as unbuckled beam instead of buckled (curved) beam since we focus on studying cubic nonlinearity only. A schematic diagram of the unit cell is depicted in Fig. 12. The unit cell is assumed to be excited in the longitudinal direction (e.g., 1D model). First, we conduct stationary analyses to check the nonlinear stiffness of the local resonator in our model. We apply a static force at the middle point of the resonator and record the displacement as the force varies. The material is selected to be Aluminum which has a density of 2700 kg/m^3 and a modulus of elasticity of 69 GPa . The out of plane thickness for the proposed structure is 4.8 mm . The displacement–force curve obtained by COMSOL is plotted in Fig. 13. To obtain the stiffness coefficient, we fit the data using MATLAB curve fitting tool. Using a formula with a linear and cubic term, we obtain the linear stiffness as 18.19 N/mm and the nonlinear cubic stiffness as 12.01 N/mm^3 with **R-squared** value near 1. The nonlinear displacement–force function for the local resonator is shown in Fig. 13. This function indicates that our assumption about weak cubic nonlinearity in the proposed model is valid. Therefore, our design is qualitatively equivalent to the original model that we investigated in the previous sections. It is noteworthy that we neglect the piezoelectric layer in the model since we only consider the weak electromechanical coupling case where its effect was shown to be negligible through this paper and in the literature [58]. However, the piezoelectric layer will be considered in the experimental demonstration in the next section.

Since the goal of the current study is to demonstrate the significant frequency shift in the long-wavelength limit (i.e., frequencies associated with relatively small wavenumbers), the corresponding frequency range of interest needs to be determined. We obtain first the linear band structure of the unit cell using COMSOL Multiphysics and plot it in Fig. 14. The waves propagating in the longitudinal direction are plotted in red stars. The bandgap for the longitudinal waves is observed around the linear in-plane natural frequency (the in plane natural frequency was determined in COMSOL Multiphysics and it is equal to 543.64 Hz) and highlighted in the shaded area in the figure. Particularly, the bandgap is located between $504.6\text{--}544.5 \text{ Hz}$. Therefore, the frequencies corresponding to the long-wavelength limit in the optical mode can be determined in the frequency region just above the bandgap. The frequency of interest in the current study is confined within the green box highlighted in Fig. 14. To further demonstrate the bandgap, we determine the transmissible curve of a chain consists of 50 cells and excited in the longitudinal direction. The transmission diagram is depicted in Fig. 15 and indicates clearly a significant drop in the transmissibility around the bandgap frequencies. Similarly, we highlight the frequency region of interest that corresponds to the long-wavelength limit in the optical mode inside the green window in Fig. 15. These frequencies are located just above the bandgap generated by mode hybridization due to local resonator. It is noteworthy that several studies in the literature have proved that the effect of nonlinearity in this region due to chain nonlinearity is negligible in this region [44], unlike the case of nonlinear local resonators investigated in the current study.

After demonstrating the bandgap in the infinite and finite structure (i.e., 50 cells chain), we conduct further nonlinear time dependent analyses using COMSOL Multiphysics. We excite the system by an input wave at a frequency, which lies within the long-wavelength limit (a frequency just after the bandgap in the optical mode). We selected this frequency to be $\omega=600 \text{ Hz}$ and defined the input wave as

$$u_0 = \frac{U_0}{2} (H(t) - H(t - 2\pi Ncy/\omega))(1 - \cos(\omega t/Ncy))\sin(\omega t) \quad (54)$$

where $H(t)$ is the Heaviside function, and Ncy is the number of cycles in the input wave and it is equal to 30 in the current simulations. We first excite the system by a low wave amplitude $U_0 = 10 \mu\text{m}$ to

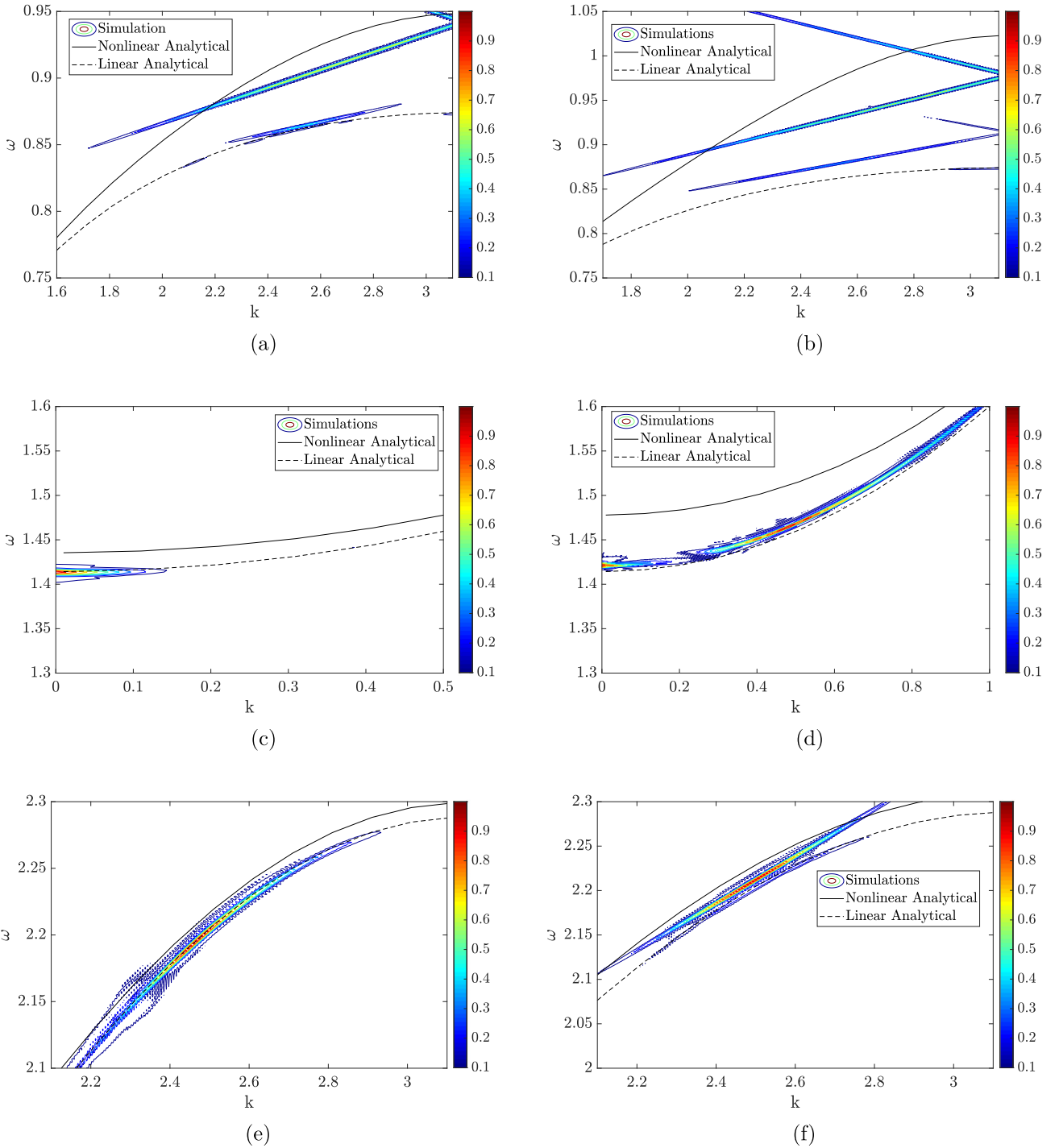


Fig. 11. Validation of the analytical results using the reconstructed dispersion curves from 2D FFT $R = 10^7$, Ω , $\theta = 10^{-8}$ N/V, $\epsilon\mu_1 = \epsilon\mu_2 = 0$: (a) Acoustics mode, $k = 7\pi/9$, $\epsilon a a^2 = 0.03$; (b) Acoustics mode, $k = 7\pi/9$, $\epsilon a a^2 = 0.06$; (c) Optical mode, $k = \pi/9$, $\epsilon a a^2 = 0.01$; (d) Optical mode, $k = \pi/9$, $\epsilon a a^2 = 0.03$; (e) Optical mode, $k = 7\pi/9$, $\epsilon a a^2 = 0.03$; (f) Optical mode, $k = 7\pi/9$, $\epsilon a a^2 = 0.06$.

investigate the behavior in the linear regime. The spectrogram of the short term Fourier transform for the temporal domain is depicted in Fig. 16(a). The results indicate that the output wave has frequency content within the input frequency range. However, a frequency component with very low energy content appears at frequency above the input frequency range. This component is developed due to the extremely weak nonlinearity at this level of input wave's amplitude. Next, we excite our structure by a large amplitude wave $U_0 = 100 \mu\text{m}$ to reach the weekly nonlinear regime. The spectrogram of the output wave is shown in Fig. 16 (b). The results indicate the existence of high

energy frequency components at frequency away from the input signal frequency. These components are generated by the appearance of second harmonic due to the nonlinearity in the local resonator [34]. This demonstrates a significant frequency shift at the long-wavelength limit, which corroborates the analytical observations in the previous sections. Increasing the vibration amplitude further will result in further migration of the energy content to frequency components away from the input frequency component and diminishing the energy content of the linear component (i.e., component with frequency equal to the input frequency).

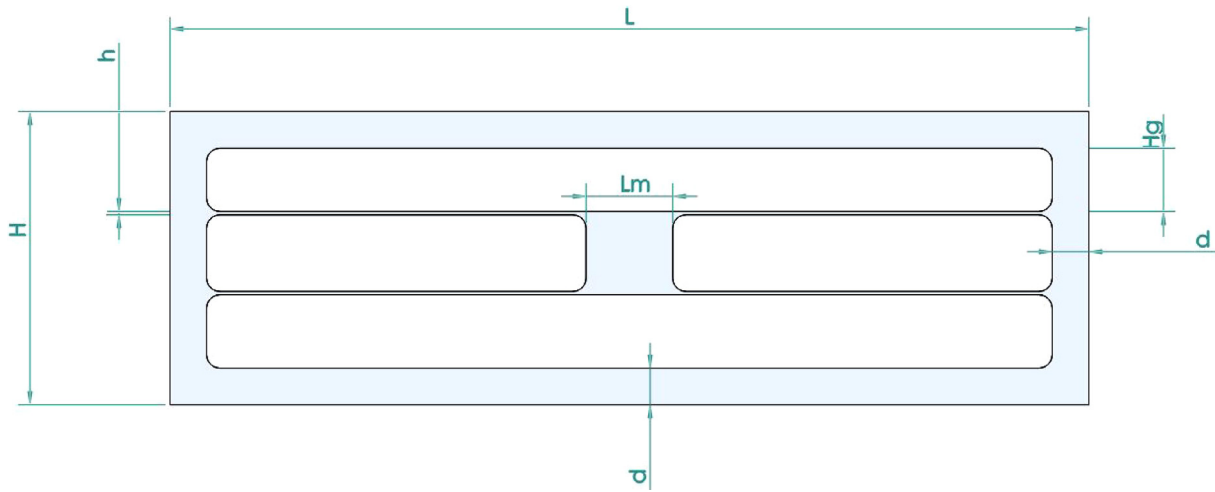


Fig. 12. A schematic for unit cell model simulated in COMSOL Multiphysics, $L = 69$ mm, $H = 22$ mm, $h = 1$ mm, $d = 2.75$ mm, $L_m = 6.5$ mm, $H_g = 5$ mm.

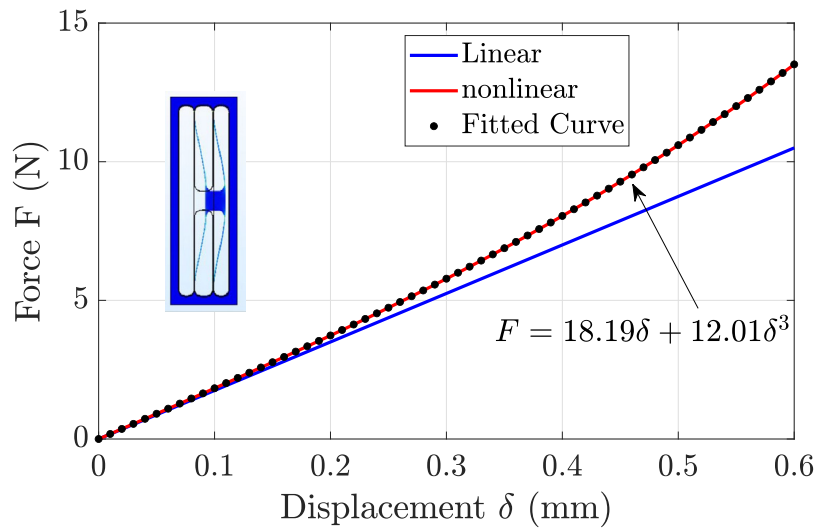


Fig. 13. Determining the resonator nonlinear stiffness for the model; displacement–force curve measured in COMSOL and fitted curve.

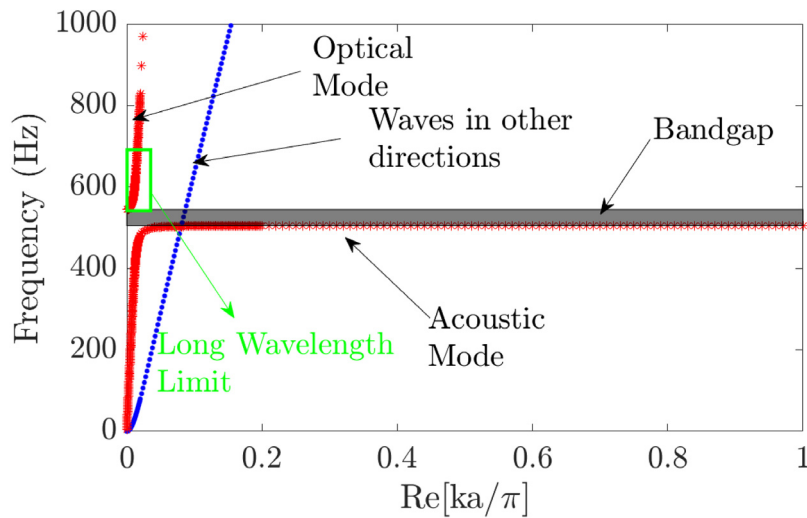


Fig. 14. Band diagram of the structure by applying periodic boundary condition in COMSOL Multiphysics. Only the Brillouin zone of the longitudinal waves is considered here. (For interpretation of the references to color in this figure legend, the reader is referred to the web version of this article.)

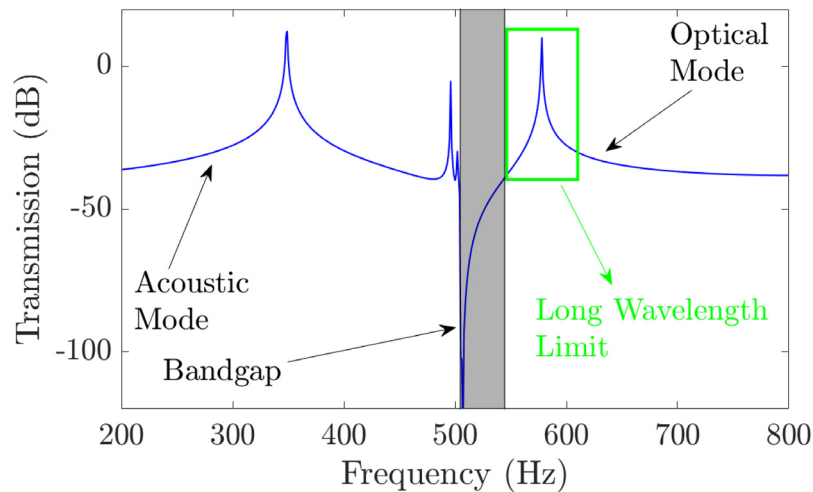


Fig. 15. Transmission diagram of a structure consisting of 50 cells. (For interpretation of the references to color in this figure legend, the reader is referred to the web version of this article.)

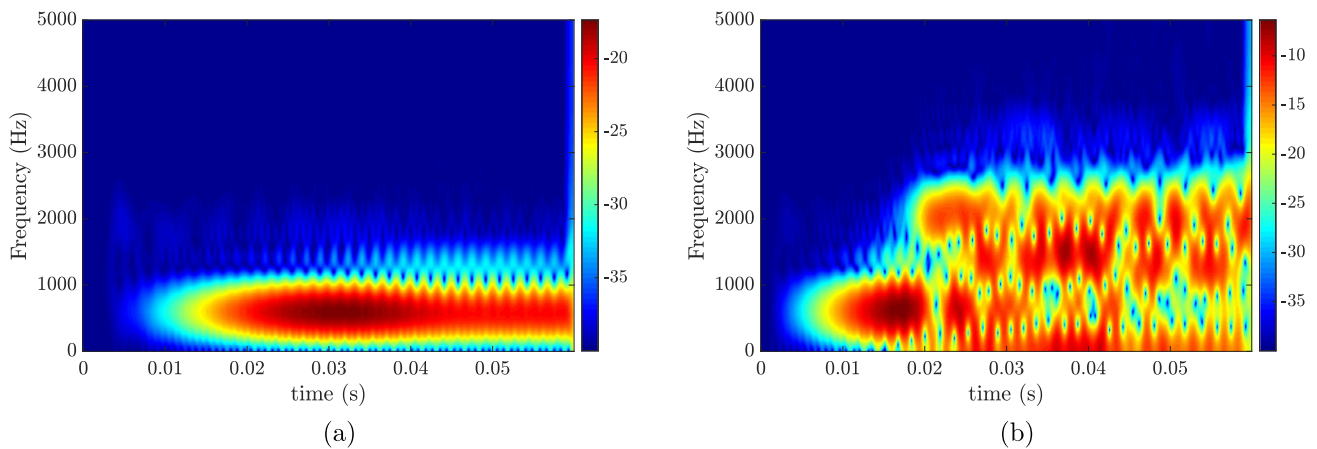


Fig. 16. Spectrogram of the short term Fourier transform for the output wave: (a) Linear regime $U_0 = 5 \mu\text{m}$; (b) Nonlinear regime $U_0 = 50 \mu\text{m}$.

7. Experimental demonstration of significant frequency shift

A metastructure prototype consists of 50 cells (i.e., single cell is shown in Fig. 12) was fabricated from Multipurpose 6061 Aluminum Sheet with a thickness of 4.8 mm. A thin piezoelectric layer was installed on the resonator embedded in the last cell to simulate the weak electromechanical coupling and monitor the harvested voltage. To simulate a free condition at the top and the bottom, the metastructure is suspended using fishing wires, as shown in Fig. 17. The first cell of the metastructure is glued to an electromagnetic shaker (LDS V408) that is driven by an amplified signal generated through the analyzer (Polytec DAQ) according to the input wave profile defined in Eq. (54). This signal is further amplified using an amplifier (LPA100). The response of the free end of the structure is recorded using Polytec Laser Doppler Vibrometer (Polytec PSV-500). In addition, the piezoelectric layer is shunted to a load resistor (2.2 M Ω) and the voltage is recorded using a DAQ system.

We first determine the transmission of the metastructure to obtain the range of frequencies of interest (i.e., the long-wavelength limit, frequencies related to small wavenumbers) that needs to be applied to the structure to demonstrate the significant frequency shift demonstrated in the current study. A burst random signal with 15 averages is used to obtain the transmission curve. The obtained transmission curve is shown in Fig. 18 and compared with COMSOL results. From the figure, it can be observed that there is a clear local resonance transmission dip at around 462 Hz. Due to some imperfection in the

manufacturing process, the experimental attenuation dip is slightly different from that of the computational with around 9% percentage error. This shift in the frequency value can also be attributed to gluing the structure to the shaker unlike the free-free boundary conditions used in the computational simulations. Moreover, this shift might also be attributed due to the holes made in the structure in order to facilitate the manufacturing process. Based on this, we also anticipate shifting the long wavelength limit to a lower frequency region. Although there are small quantitative discrepancies between the designed analytical model and the fabricated structure, both models are qualitatively equivalent since they both demonstrate a local resonant bandgap. Consequently, one can follow the analyses presented in the previous section to locate the range of frequencies of interest (i.e., the long-wavelength limit, frequencies related to small wavenumbers) in the current study. Therefore, one can safely locate the frequencies corresponding to the long-wavelength limit in the optical mode in the region of frequencies just above the bandgap upper boundary. A portion of this frequency region is highlighted inside the green window in Fig. 18. Therefore, we select 530 Hz as an excitation frequency to demonstrate the frequency shift in the long-wavelength limit.

Next, we applied an input wave with a frequency of 530 Hz and 30 cycles to the structure and measure the harvested voltage. The measured voltage is further analyzed by determining the short term Fourier transform of the signal, as shown in Fig. 19. At low amplitude input signal (i.e., 0.05 V, 0.1269 g), the results indicate that the harvested voltage is confined within the input frequency region and no

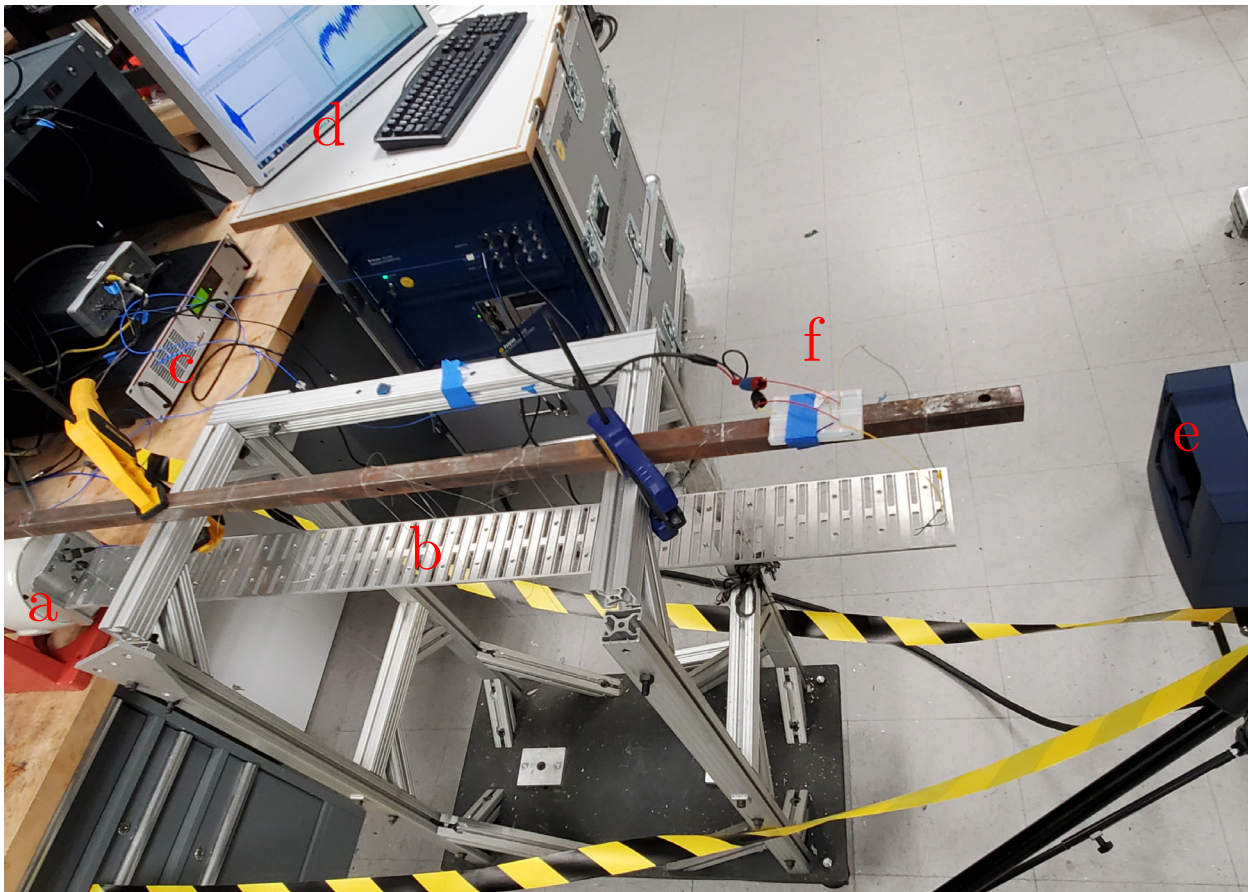


Fig. 17. Experimental setup of the metastructure prototype: (a) Shaker, (b) prototype, (c) amplifier, (d) analyzer, (e) laser doppler, (f) shunted circuit.

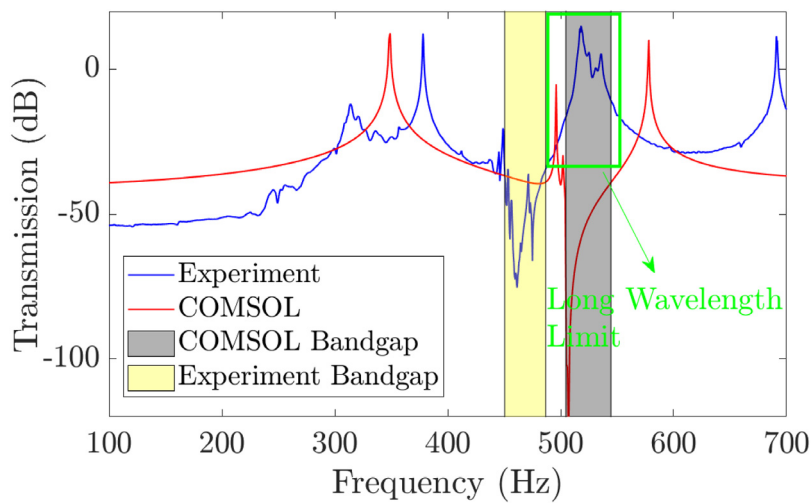


Fig. 18. Experimental transmission diagram of a structure consists of 50 cells. (For interpretation of the references to color in this figure legend, the reader is referred to the web version of this article.)

frequency shift can be observed, as depicted in Fig. 19(a). This indicates that the metastructure is excited in the linear regime where the effect of nonlinearity is negligible. However, when we increase the input voltage to 0.5 V, multiple frequency components appear at frequencies different from the input frequency range with a significant energy content, as shown in Fig. 19(b). Indeed, this clearly demonstrates the significant frequency shift at the long-wavelength limit due to resonator nonlinearity when the system is excited in the nonlinear regime. In addition, this observation supports the qualitative agreement between the

design computational model and the fabricated structure in locating the long-wavelength limit region and the dominant source of nonlinearity, which is the local resonator nonlinearity. This is because the effect of nonlinearity due to chain nonlinearity is negligible in this region and it cannot lead to any frequency shift [44,64], unlike the frequency shift obtained by the experimental results here. Hence, the experimental observation corroborates qualitatively both the analytical and computational findings i.e., the emergence of significant frequency shift in the long-wavelength domain. The observed significant frequency shift may

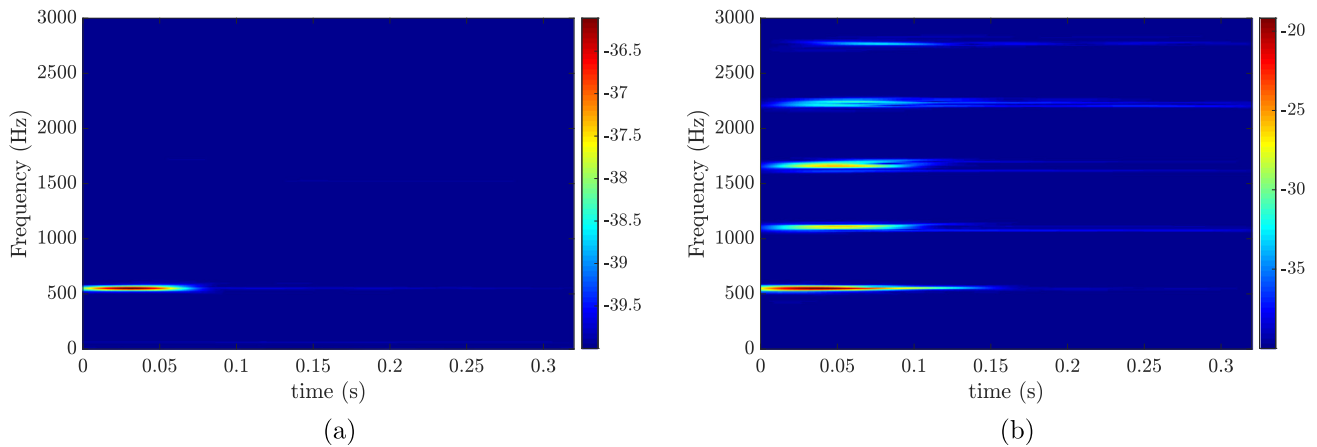


Fig. 19. Spectrogram of the short term Fourier transform for the measured output voltage: (a) Linear regime 0.05 Volt; (b) Nonlinear regime 0.5 Volt.

be attributed by second harmonic generation due to the nonlinearity in the local resonator [34]. Therefore, these components with shifted frequency content can be utilized to design the electromechanical diode when coupled to a linear chain.

8. Conclusion

In this paper, we investigated a metamaterial with nonlinear local electromechanical resonators for simultaneous energy harvesting and vibration attenuation. The metamaterial consists of a chain of masses connected by linear springs. A weakly nonlinear electromechanical resonator was coupled to each cell and shunted to a load resistor to harvest energy. The model of the electromechanical resonator was reduced to an equivalent nonlinear spring–mass system with an equivalent capacitance of the piezoelectric element and an equivalent coupling coefficient. An approximate closed-form solution for the dispersion relation was obtained by MMS. The analytical results indicated that the effect of nonlinearity is more pronounced at frequencies close to the resonance frequency of the electromechanical resonator. Therefore, it can appear at all wavelength limits, unlike the case of chain nonlinearity, where the effect of nonlinearity was concentrated at the medium-wavelength limit only. Moreover, the results demonstrated that weakly electromechanical coupling has no effect on the bandgap size and dispersion curves. The electromechanical coupling affects only the attenuation level inside the bandgap without changing its size. Therefore, the proposed system can also be employed in energy harvesting applications without degrading the obtained bandgap size. On the other hand, a very strong electromechanical coupling can lead to a significant change in the band structure and merge the apart acoustics and optical mode into one dispersion curve.

To reveal more important characteristics of the nonlinear wave propagation in the proposed structure other than the cut-off frequencies, we conducted signal processing techniques on the numerical results to investigate the spectro-spatial features. The spatial wave profile of the signals demonstrated that propagating waves are subjected to severe wave distortion at all wavelength limits in the case of the nonlinear electromechanical resonator. In general, the effect of softening nonlinearity appears as a wave stretching over the chain, while the effect of hardening nonlinearity appears as traveling localized component. The severity of wave distortion was significant at excitation frequencies close to the resonance frequency of the electromechanical resonator. In the acoustics mode, it was demonstrated that the traveling localized component has a harvested voltage higher than the linear case, thus hardening nonlinearity of the resonator can enhance sensing. The STFT also demonstrated the wave localization/stretching due to the hardening/softening nonlinearity at the medium and the short-wavelength limits in the acoustics mode and at the short wave length limit in

the optical mode. However, the results demonstrated a significant frequency shift at medium-wavelength limit in the optical mode for both types of nonlinearity. In particular, the output frequency components of the wave appeared at frequencies different than the input frequency and the energy content was concentrated into multiple component. Unlike the case of nonlinear chain, the nonlinearity in the electromechanical resonator surprisingly showed a significant frequency shift at long-wavelength limit in the optical mode. This frequency shift can extend the application of metamaterials to the long-wavelength region in addition to medium and short-wavelengths. Furthermore, we obtained the contour plot of 2D FFT to numerically reconstruct the dispersion curves. In addition to demonstrating the significant frequency shift, the results demonstrated that hardening nonlinearity has a localized component with a fix slope. This indicated that the localized traveling component is a solitary wave. Furthermore, we employed the contour plots to validate our analytical solution. The results demonstrated the limitations of the obtained analytical solution. Although our analytical solution showed a limitation in predicting the cut-off frequency, it can be effectively used in obtaining the most affected regions and wavelength limits by nonlinearity. Finally, we proved qualitatively the existence of significant frequency shift computationally using COMSOL Multiphysics and experimentally. We designed a cell with weak cubic nonlinearity. Upon exciting a chain of 50 cells at the long-wavelength limit, we were able to show a significant frequency shift in this limit with large amplitude waves.

CRedit authorship contribution statement

Mohammad Bukhari: Conceptualization, Methodology, Software, Data curation, Writing – original draft, Investigation. **Oumar Barry:** Supervision, Validation, Writing – review & editing, Conceptualization, Methodology.

Declaration of competing interest

The authors declare that they have no known competing financial interests or personal relationships that could have appeared to influence the work reported in this paper.

Acknowledgments

This work was supported in part by the National Science Foundation (NSF) under Grant number CMMI-2038187.

References

- [1] Mahmoud I. Hussein, Michael J. Leamy, Massimo Ruzzene, Dynamics of phononic materials and structures: Historical origins, recent progress, and future outlook, *Appl. Mech. Rev.* 66 (4) (2014) 040802.
- [2] Katia Bertoldi, Vincenzo Vitelli, Johan Christensen, Martin van Hecke, Flexible mechanical metamaterials, *Nat. Rev. Mater.* 2 (11) (2017) 17066.
- [3] Wenshan Cai, Vladimir M. Shalaev, *Optical Metamaterials*, Vol. 10, no. 6011, Springer, 2010.
- [4] Rosa Martínez-Sala, J. Sancho, Juan V. Sánchez, Vicente Gómez, Jaime Llinares, Francisco Meseguer, Sound attenuation by sculpture, *Nature* 378 (6554) (1995) 241.
- [5] Michael M. Sigalas, Eleftherios N. Economou, Elastic and acoustic wave band structure, *J. Sound Vib.* 158 (1992) 377–382.
- [6] Zhengyou Liu, Xixiang Zhang, Yiwei Mao, Y.Y. Zhu, Zhiyu Yang, Che Ting Chan, Ping Sheng, Locally resonant sonic materials, *Science* 289 (5485) (2000) 1734–1736.
- [7] M. Sigalas, Eleftherios N. Economou, Band structure of elastic waves in two dimensional systems, *Solid State Commun.* 86 (3) (1993) 141–143.
- [8] Manvir S. Kushwaha, Peter Halevi, Leonard Dobrzynski, Bahram Djafari-Rouhani, Acoustic band structure of periodic elastic composites, *Phys. Rev. Lett.* 71 (13) (1993) 2022.
- [9] Manvir S. Kushwaha, P. Halevi, G. Martinez, Leonard Dobrzynski, Bahram Djafari-Rouhani, Theory of acoustic band structure of periodic elastic composites, *Phys. Rev. B* 49 (4) (1994) 2313.
- [10] J.O. Vasseur, B. Djafari-Rouhani, L. Dobrzynski, M.S. Kushwaha, P. Halevi, Complete acoustic band gaps in periodic fibre reinforced composite materials: The carbon/epoxy composite and some metallic systems, *J. Phys.: Condens. Matter* 6 (42) (1994) 8759.
- [11] Manvir S. Kushwaha, Classical band structure of periodic elastic composites, *Internat. J. Modern Phys. B* 10 (09) (1996) 977–1094.
- [12] Liao Liu, Mahmoud I. Hussein, Wave motion in periodic flexural beams and characterization of the transition between bragg scattering and local resonance, *J. Appl. Mech.* 79 (1) (2012) 011003.
- [13] Younes Achaoui, Vincent Laude, Sarah Benhabane, Abdelkrim Khelif, Local resonances in phononic crystals and in random arrangements of pillars on a surface, *J. Appl. Phys.* 114 (10) (2013) 104503.
- [14] G.L. Huang, C.T. Sun, Band gaps in a multiresonator acoustic metamaterial, *J. Vib. Acoust.* 132 (3) (2010) 031003.
- [15] R. Zhu, X.N. Liu, G.K. Hu, C.T. Sun, G.L. Huang, A chiral elastic metamaterial beam for broadband vibration suppression, *J. Sound Vib.* 333 (10) (2014) 2759–2773.
- [16] Ali H. Nayfeh, *Introduction to Perturbation Techniques*, John Wiley & Sons, 2011.
- [17] Ali H. Nayfeh, Dean T. Mook, *Nonlinear Oscillations*, John Wiley & Sons, 2008.
- [18] Raj K. Narisetti, Michael J. Leamy, Massimo Ruzzene, A perturbation approach for predicting wave propagation in one-dimensional nonlinear periodic structures, *J. Vib. Acoust.* 132 (3) (2010) 031001.
- [19] Kevin Manktelow, Michael J. Leamy, Massimo Ruzzene, Comparison of asymptotic and transfer matrix approaches for evaluating intensity-dependent dispersion in nonlinear photonic and phononic crystals, *Wave Motion* 50 (3) (2013) 494–508.
- [20] Kevin L. Manktelow, Michael J. Leamy, Massimo Ruzzene, Analysis and experimental estimation of nonlinear dispersion in a periodic string, *J. Vib. Acoust.* 136 (3) (2014).
- [21] Kevin Manktelow, Michael J. Leamy, Massimo Ruzzene, Multiple scales analysis of wave-wave interactions in a cubically nonlinear monoatomic chain, *Nonlinear Dynam.* 63 (1–2) (2011) 193–203.
- [22] Matthew D. Fronk, Michael J. Leamy, Higher-order multiple scales analysis of weakly nonlinear lattices with implications for directional stability, in: *International Design Engineering Technical Conferences and Computers and Information in Engineering Conference*, Vol. 51852, American Society of Mechanical Engineers, 2018, V008T10A001.
- [23] R.K. Narisetti, M. Ruzzene, M.J. Leamy, A perturbation approach for analyzing dispersion and group velocities in two-dimensional nonlinear periodic lattices, *J. Vib. Acoust.* 133 (6) (2011).
- [24] Kevin Manktelow, Raj K. Narisetti, Michael J. Leamy, Massimo Ruzzene, Finite-element based perturbation analysis of wave propagation in nonlinear periodic structures, *Mech. Syst. Signal Process.* 39 (1–2) (2013) 32–46.
- [25] Raj Kumar Pal, Federico Bonetto, Luca Dieci, Massimo Ruzzene, A study of deformation localization in nonlinear elastic square lattices under compression, *Phil. Trans. R. Soc. A* 376 (2127) (2018) 20170140.
- [26] Matthew D. Fronk, Michael J. Leamy, Direction-dependent invariant waveforms and stability in two-dimensional, weakly nonlinear lattices, *J. Sound Vib.* 447 (2019) 137–154.
- [27] Romik Khajetourian, Mahmoud I. Hussein, Dispersion characteristics of a nonlinear elastic metamaterial, *Aip Adv.* 4 (12) (2014) 124308.
- [28] Mohammad H. Abedinnasab, Mahmoud I. Hussein, Wave dispersion under finite deformation, *Wave Motion* 50 (3) (2013) 374–388.
- [29] Mohammad H. Abedin-Nasab, Mary V. Bastawrous, Mahmoud I. Hussein, Explicit dispersion relation for strongly nonlinear flexural waves using the homotopy analysis method, *Nonlinear Dynam.* 99 (1) (2020) 737–752.
- [30] Yuri S. Kivshar, Nikos Flytzanis, Gap solitons in diatomic lattices, *Phys. Rev. A* 46 (12) (1992) 7972.
- [31] Neel Nadkarni, Chiara Daraio, Dennis M. Kochmann, Dynamics of periodic mechanical structures containing bistable elastic elements: From elastic to solitary wave propagation, *Phys. Rev. E* 90 (2) (2014) 023204.
- [32] Bin Liang, Bo Yuan, Jian-chun Cheng, Acoustic diode: Rectification of acoustic energy flux in one-dimensional systems, *Phys. Rev. Lett.* 103 (10) (2009) 104301.
- [33] Amir Darabi, Lezheng Fang, Alireza Mojahed, Matthew D. Fronk, Alexander F. Vakakis, Michael J. Leamy, Broadband passive nonlinear acoustic diode, *Phys. Rev. B* 99 (21) (2019) 214305.
- [34] Weijian Jiao, Stefano Gonella, Doubly nonlinear waveguides with self-switching functionality selection capabilities, *Phys. Rev. E* 99 (4) (2019) 042206.
- [35] Weijian Jiao, Stefano Gonella, Nonlinear harmonic generation in two-dimensional lattices of repulsive magnets, *Phys. Rev. E* 103 (1) (2021) 012123.
- [36] James M. Manimala, C.T. Sun, Numerical investigation of amplitude-dependent dynamic response in acoustic metamaterials with nonlinear oscillators, *J. Acoust. Soc. Am.* 139 (6) (2016) 3365–3372.
- [37] Xin Fang, Jihong Wen, Jianfei Yin, Dianlong Yu, Yong Xiao, Broadband and tunable one-dimensional strongly nonlinear acoustic metamaterials: Theoretical study, *Phys. Rev. E* 94 (5) (2016) 052206.
- [38] Xin Fang, Jihong Wen, Dianlong Yu, Jianfei Yin, Bridging-coupling band gaps in nonlinear acoustic metamaterials, *Phys. Rev. A* 10 (5) (2018) 054049.
- [39] Arnab Banerjee, Emilio P. Calius, Raj Das, An impact based mass-in-mass unit as a building block of wideband nonlinear resonating metamaterial, *Int. J. Non-Linear Mech.* 101 (2018) 8–15.
- [40] Yiwei Xia, Massimo Ruzzene, Alper Erturk, Dramatic bandwidth enhancement in nonlinear metastructures via bistable attachments, *Appl. Phys. Lett.* 114 (9) (2019) 093501.
- [41] Yi-Ze Wang, Yue-Sheng Wang, Active control of elastic wave propagation in nonlinear phononic crystals consisting of diatomic lattice chain, *Wave Motion* 78 (2018) 1–8.
- [42] Soroush Sepehri, Mahmoud Mosavi Mashhadi, Mir Masoud Seyyed Fakhrebadi, Dispersion curves of electromagnetically actuated nonlinear monoatomic and mass-in-mass lattice chains, *Int. J. Mech. Sci.* 214 (2022) 106896.
- [43] R. Ganesh, Stefano Gonella, Spectro-spatial wave features as detectors and classifiers of nonlinearity in periodic chains, *Wave Motion* 50 (4) (2013) 821–835.
- [44] W.J. Zhou, X.P. Li, Y.S. Wang, W.Q. Chen, G.L. Huang, Spectro-spatial analysis of wave packet propagation in nonlinear acoustic metamaterials, *J. Sound Vib.* 413 (2018) 250–269.
- [45] Mohammad A. Bukhari, Oumar R. Barry, Spectro-spatial analyses of a nonlinear metamaterial with multiple nonlinear local resonators, *Nonlinear Dynam.* (2019).
- [46] Mohammad A. Bukhari, Oumar R. Barry, Nonlinear metamaterials with multiple local mechanical resonators: Analytical and numerical analyses, in: *NODYCON 2019 the First International Nonlinear Dynamics Conference*, 2019.
- [47] Mohammad Bukhari, Oumar Barry, On the spectro-spatial wave features in nonlinear metamaterials with multiple local resonators, in: *ASME 2018 International Design Engineering Technical Conferences and Computers and Information in Engineering Conference*, American Society of Mechanical Engineers, 2019.
- [48] Li Shen, Jiu Hui Wu, Siwen Zhang, Zhangyi Liu, Jing Li, Low-frequency vibration energy harvesting using a locally resonant phononic crystal plate with spiral beams, *Modern Phys. Lett. B* 29 (01) (2015) 1450259.
- [49] Guobiao Hu, Lihua Tang, Arnab Banerjee, Raj Das, Metastucture with piezoelectric element for simultaneous vibration suppression and energy harvesting, *J. Vib. Acoust.* 139 (1) (2017) 011012.
- [50] O. Thorp, Massimo Ruzzene, A. Baz, Attenuation and localization of wave propagation in rods with periodic shunted piezoelectric patches, *Smart Mater. Struct.* 10 (5) (2001) 979.
- [51] L. Airoldi, M. Ruzzene, Wave propagation control in beams through periodic multi-branch shunts, *J. Intell. Mater. Syst. Struct.* 22 (14) (2011) 1567–1579.
- [52] Filippo Casadei, Tommaso Delpero, Andrea Bergamini, Paolo Ermanni, Massimo Ruzzene, Piezoelectric resonator arrays for tunable acoustic waveguides and metamaterials, *J. Appl. Phys.* 112 (6) (2012) 064902.
- [53] Andrea Bergamini, Tommaso Delpero, Luca De Simoni, Luigi Di Lillo, Massimo Ruzzene, Paolo Ermanni, Phononic crystal with adaptive connectivity, *Adv. Mater.* 26 (9) (2014) 1343–1347.
- [54] Wanlu Zhou, You Wu, Lei Zuo, Vibration and wave propagation attenuation for metamaterials by periodic piezoelectric arrays with high-order resonant circuit shunts, *Smart Mater. Struct.* 24 (6) (2015) 065021.
- [55] Guobiao Hu, Lihua Tang, Raj Das, Metamaterial-inspired piezoelectric system with dual functionalities: Energy harvesting and vibration suppression, in: *Active and Passive Smart Structures and Integrated Systems 2017*, Vol. 10164, International Society for Optics and Photonics, 2017, p. 101641X.
- [56] Guobiao Hu, Lihua Tang, Raj Das, Internally coupled metamaterial beam for simultaneous vibration suppression and low frequency energy harvesting, *J. Appl. Phys.* 123 (5) (2018) 055107.

- [57] Ying Li, Evan Baker, Timothy Reissman, Cheng Sun, Wing Kam Liu, Design of mechanical metamaterials for simultaneous vibration isolation and energy harvesting, *Appl. Phys. Lett.* 111 (25) (2017) 251903.
- [58] Mohammad Bukhari, Omar Barry, Simultaneous energy harvesting and vibration control in a nonlinear metastructure: A spectro-spatial analysis, *J. Sound Vib.* 473 (2020) 115215.
- [59] Alper Erturk, Daniel J. Inman, *Piezoelectric Energy Harvesting*, John Wiley & Sons, 2011.
- [60] Mahmoud I. Hussein, Michael J. Frazier, Metadamping: An emergent phenomenon in dissipative metamaterials, *J. Sound Vib.* 332 (20) (2013) 4767–4774.
- [61] Mahmoud I. Hussein, Michael J. Frazier, Band structure of phononic crystals with general damping, *J. Appl. Phys.* 108 (9) (2010) 093506.
- [62] M.I. Hussein, R. Khajetourian, Nonlinear Bloch waves and balance between hardening and softening dispersion, *Proc. Royal Soc. A* 474 (2217) (2018) 20180173.
- [63] Valentina Zega, Priscilla B. Silva, Marc G.D. Geers, Varvara G. Kouznetsova, Experimental proof of emergent subharmonic attenuation zones in a nonlinear locally resonant metamaterial, *Sci. Rep.* 10 (1) (2020) 1–11.
- [64] Matthew D. Fronk, Michael J. Leamy, Isolated frequencies at which nonlinear materials behave linearly, *Phys. Rev. E* 100 (5) (2019) 051002.